nature water

Supplementary information

https://doi.org/10.1038/s44221-026-00734-6

Solar-operated interlayer electrothermal evaporator enabling instant high-flux freshwater production across multiple scenarios

In the format provided by the authors and unedited

Table of Contents

Supplementary Notes 1

Supplementary Note 1. Sectional temperature distribution of interlayer heating mechanism. 1

Supplementary Note 2. Preparation of p-rGO ink and p-rGO/WC ink. 2

Supplementary Note 3. Calculation of apparent heat loss. 3

Supplementary Note 4. Calculation of apparent energy efficiency of IEE and solar-operated IEE. 4

Supplementary Note 5. Energy analysis of solar-operated IEE. 6

Supplementary Note 6. Calculation of energy utilization efficiency of solar-operated IEE. 9

Supplementary Note 7. Theoretical calculation. 11

Supplementary Note 8. Calculation of rejection. 12

Supplementary Note 9. Measurement of salt transport flux. 12

Supplementary Note 10. Measurement of water transport rate. 13

Supplementary Note 11. Outdoor experiments of solar-operated IEE. 13

Supplementary Note 12. Analysis of freshwater production process.. 14

Supplementary Figures 16

Supplementary Figure 1. Schematic of the IEE composed of different components. 16

Supplementary Figure 2. Infrared thermal images of different metal meshes at 0.5 V. 17

Supplementary Figure 3. Characterization of the TiG mesh. 18

Supplementary Figure 4. Infrared thermal images of the TiG mesh with electrode. 19

Supplementary Figure 5. Electrothermal properties of TiG mesh. 20

Supplementary Figure 6. Fabrication and characterization of the rGO TC. 21

Supplementary Figure 7. Fabrication of the rGO-WC EI. 22

Supplementary Figure 8. Morphology of the rGO-WC EI. 23

Supplementary Figure 9. Characterization of the rGO-WC EI. 24

Supplementary Figure 10. Absorption of the rGO-WC EI. 25

Supplementary Figure 11. Photothermal properties of rGO-WC EI. 26

Supplementary Figure 12. Electrothermal performance of the IEE. 27
Supplementary Figure 13. Electrothermal performance of the electrothermal evaporator with the EL at the top or bottom. 28
Supplementary Figure 14. Comparison of evaporation rate between IEE and traditional electrothermal evaporators at driving voltage..... 29
Supplementary Figure 15. Heat loss of BEE, IFEE, and IEE at 1.5 V. 30
Supplementary Figure 16. Energy consumption of BEE and IEE at 1.5 V for evaporating 5 g of brine. 31
Supplementary Figure 17. Temperature changes of bulk brine in BEE and IEE. 32
Supplementary Figure 18. Evaporation rate comparison between the IEE and previously reported electrothermal desalination technologies at unit voltage..... 33
Supplementary Figure 19. Photothermal performance of the IEE under different light intensities. 34
Supplementary Figure 20. Photothermal electrothermal coupling performance of the solar-operated IEE. 35
Supplementary Figure 21. Schematic of the heat transfer model for solar-operated IEE. 36
Supplementary Figure 22. Cross-sectional infrared thermal images and temperature distribution of the solar-operated IEE and BEE under 20 $kW \cdot m^{-2}$ illumination and at the voltage of 1.5 V. 37
Supplementary Figure 23. Schematic of heat loss of BEE and IEE under electrothermal-photothermal conditions. 38
Supplementary Figure 24. Computation module of COMSOL simulations..... 39
Supplementary Figure 25. COMSOL simulations of BEE, IFEE, and IEE. 40
Supplementary Figure 26. Performance comparison of the BEE, the IFEE, and the IEE in many aspects. 41
Supplementary Figure 27. Freshwater production phenomenon of the solar-operated IEE under 20 $kW \cdot m^{-2}$ illumination and at the voltage of 1.5 V. 42
Supplementary Figure 28. Freshwater flux of IEE and BEE at 1.5 V. 43
Supplementary Figure 29. Freshwater flux of the solar-operated IEE and solar-operated BEE. 44

Supplementary Figure 30. Concentration changes in 3.5 wt% NaCl before and after solar desalination. 45
Supplementary Figure 31. Ion concentrations and rejction of IEE. 46
Supplementary Figure 32. Photographs of the solar-operated IEE during tests at different periods under 20 kW·m^{-2} illumination and at a voltage of 1.5 V. 47
Supplementary Figure 33. Salt transport flux of the IEE. 48
Supplementary Figure 34. Photographs of water transport in IEE. 49
Supplementary Figure 35. SEM images and corresponding elemental mapping before and after test. 50
Supplementary Figure 36. XRD patterns before and after test. 51
Supplementary Figure 37. XPS spectra before and after test. 52
Supplementary Figure 38. Water contact angle before and after test. 53
Supplementary Figure 39. Comparison of photothermal-electrothermal coupled evaporation rate between the solar-operated IEE (1.5 V with 1 kW·m^{-2} and 20 kW·m^{-2}) and other reported evaporators. 54
Supplementary Figure 40. Photographs of foldable solar cell and Fresnel lens. 55
Supplementary Figure 41. Outdoor freshwater production and sample integration. 56
Supplementary Figure 42. All-day outdoor experiment. 57
Supplementary Figure 43. Characterization of various water sources before and after desalination. 58
Supplementary Figure 44. Evaporation rate and freshwater flux of the solar-operated IEE for sediment water, oil water, high-salinity wastewater, and strong-acid water under 20 kW·m^{-2} illumination and at the voltage of 1.5 V. 59

Supplementary Tables 60

Supplementary Table 1. Freshwater flux and apparent energy efficiency comparison of the IEE versus other reported electrothermal and photothermal desalination technologies. 60
Supplementary Table 2. Comparison of evaporation rate between IEE and traditional electrothermal evaporator under different voltages. 61
Supplementary Table 3. Evaporation rate comparison between the IEE and previously

reported electrothermal desalination technologies at unit voltage..... 62
Supplementary Table 4. ICP data of ion concentration of real Bohai seawater and collected freshwater. 62
Supplementary Table 5. Comparison of photothermal-electrothermal coupled evaporation rate between IEE and other reported evaporators. 64
Supplementary Table 6. Natural light intensity and concentrated light intensity changes with time. 65
Supplementary Table 7. Comparison of freshwater flux with other reported water treatment technologies. 66
Supplementary References.....67

Supplementary Notes

Supplementary Note 1. Sectional temperature distribution of interlayer heating mechanism.

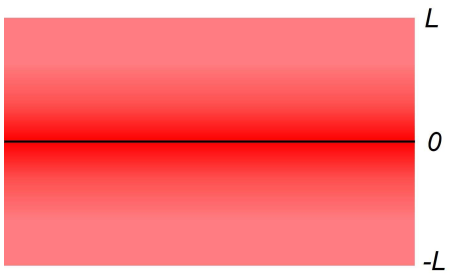


Figure 1-1. Schematic of cross-section temperature distribution when there is a uniform internal heat source in the plate.

As shown as Figure 1-1, for the plate, when there is a uniform internal heat source, the steady-state heat conduction equation is:

$$\frac{d^2T}{dx^2} = -\frac{q}{k}$$

where q is the volume heat flux density, k is the thermal conductivity of the material, T is the temperature, and x is the spatial coordinate.

The heat flux gradient is obtained by integrating the above equation once:

$$\frac{dT}{dx} = \int -\frac{q}{k}dx = -\frac{q}{k}x + C_1$$

Due to the uniform plate structure and internal heat source, the temperature distribution is symmetrical about the center $x = 0$. Therefore, at $x = 0$, the heat flux gradient is zero:

$$\frac{dT}{dx}_{x=0} = 0$$

Substitute into the equation:

$$0 = -\frac{q}{k} \cdot 0 + C_1 \rightarrow C_1 = 0$$

Therefore, the equation is simplified as:

$$\frac{dT}{dx} = -\frac{q}{k}x$$

By reintegrating the simplified equation, the temperature distribution is obtained:

$$T(x) = \int -\frac{q}{k}xdx = -\frac{q}{k} \cdot \frac{x^2}{2} + C_2$$

At the center point $x = 0$, the temperature is defined as T_{center}:

$$T(0) = T_{\text{center}}$$

Substitute into the equation:

$$T(0) = -\frac{q}{2k} \cdot 0^2 + C_2 = C_2 \rightarrow C_2 = T_{\text{center}}$$

Therefore, the temperature distribution is:

$$T(x) = T_{\text{center}} - \frac{q}{2k}x^2$$

The final formula is:

$$T(x) = T_{\text{center}} - \frac{q}{2k}x^2, -L \leq x \leq L$$

We plotted the derived formula and found that temperature varies parabolically with the distance from the heat source (Figure 1-2). This further theoretically clarifies the origin of the parabolic temperature distribution inherent to the interlayer heating mechanism.

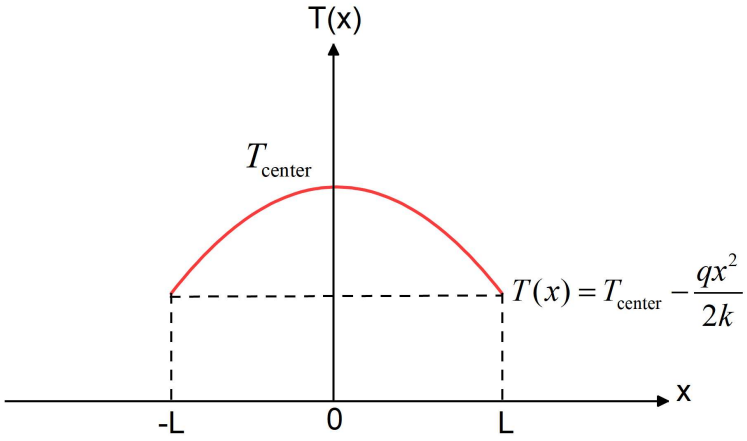


Figure 1-2. The temperature curve deduced according to the formula.

Supplementary Note 2. Preparation of p-rGO ink and p-rGO/WC ink

GO aqueous solution (2 mg·mL^{-1}) was synthesized via the modified Hummers method. Subsequently, the GO solution was reduced using ascorbic acid solution (80 mg·mL^{-1}) at 70 °C for 30 min. The p-rGO ink was obtained after suction filtration. p-rGO/WC inks were formulated by combining varying mass ratios of WC NPs, with rGO to WC NPs ratios set at 1:1, 1:2, and 1:3, respectively. All inks were thoroughly homogenized using a high-shear homogenizer.

Supplementary Note 3. Calculation of apparent heat loss

Heat loss consists of three parts: heat conduction loss, heat convection loss, and heat radiation loss.

3.1 Apparent heat conduction loss

The apparent conduction heat loss refers to the heat loss between the evaporator and the bulk brine. It was calculated according to the following equation.

$$P_{\mathrm{con}} = \frac{C \cdot m \cdot \Delta T}{S \cdot t}$$

where P_{con} is the energy of apparent heat conduction loss. C denotes the specific heat capacity of bulk water (4.18 kJ·kg^{-1}·K^{-1}), m represents the weight of bulk brine, and $\Delta T = T_2 - T_1$, T_2 is the temperature of the bulk brine when the evaporator evaporates stably, T_1 is the initial temperature of bulk brine. S is the projection area of the container, and t is the test time.

3.2 Apparent heat convection loss

Apparent convection heat loss refers to the heat loss caused by natural convection between the evaporator and the environment. It is calculated by the Newtonian cooling formula.

$$P_{\mathrm{conv}} = h \cdot \Delta T$$

where P_{conv} is the energy of the apparent convection heat loss. h denotes the convection heat transfer coefficient (5 W·m^{-2}·K^{-1}).[1] $\Delta T = T_0 - T_{\mathrm{m}}$, T_0 is the average temperature of the EI when the evaporator evaporates stably, and T_{m} is the ambient temperature.

3.3 Apparent heat radiation loss

Apparent radiant heat loss refers to the heat loss caused by heat radiation between the evaporator and the environment. It is calculated by Stefan-Boltzmann's law.

$$P_{\mathrm{rad}} = \epsilon \cdot \sigma \cdot (T_0^4 - T_{\mathrm{m}}^4)$$

where P_{rad} is the energy of the apparent radiation heat loss. ϵ represents the emissivity of the solar absorber ($\epsilon \approx 1$) and σ represents the Stefan-Boltzmann constant (5.67×10^{-8} W·m^{-2}·K^{-4}), T_0 is the average temperature of the EI when the evaporator evaporates stably, and T_{m} is the ambient temperature.

Supplementary Note 4. Calculation of apparent energy efficiency of IEE and solar-operated IEE

The IEE achieved an apparent energy efficiency of up to 93.31% under a coupled input of 20 kW·m^{-2} solar irradiation and an applied voltage of 1.5 V. This key performance metric, defined as the ratio of the energy consumed for water evaporation to the total energy input per unit projected area, is calculated via the formula below, following a standardized calculation method widely adopted in previous literature:[2,3]

$$\eta = \frac{\dot{m} \cdot \left[C_{\text{liquid}} \cdot (T_1 - T_0) + \Delta h_{\text{vapor}}\right]}{P_{\text{electricty}} + P_{\text{solar}}}$$

where η is apparent energy efficiency (%), $\dot{m}$ is evaporation rate (kg·m^{-2}·h^{-1}), C_{liquid} is specific heat capacity of water (4.18 kJ·kg^{-1}·K^{-1}), T_1 is the steady-state temperature of the evaporation interface (K), T_0 is the initial temperature of the evaporation interface (K), Δh_{vapor} is latent heat of vaporization (kJ·kg^{-1}), $P_{\text{electricty}}$ is the electrical input (kW·m^{-2}), P_{solar} is the solar energy input (kW·m^{-2}). Among them, $C_{\text{liquid}} \cdot (T_1 - T_0)$ is the sensible heat of vapor.

The latent heat of vaporization is calculated as follow:[4,5]

$$\Delta h_{\text{vapor}} = C_{\text{liquid}} \cdot (373.15 - T_1) + \Delta h_{100} + C_{\text{vapor}} \cdot (T_1 - 373.15)$$

where Δh_{vapor} is latent heat of vaporization (kJ·kg^{-1}), C_{liquid} is specific heat capacity of water (4.18 kJ·kg^{-1}·K^{-1}), T_1 is the steady-state temperature of the evaporation interface (K), Δh_{100} is the latent heat of water at 100 °C (373.15 K, taken to be 2260 kJ·kg^{-1}), and the C_{vapor} is the specific heat capacity of vapor (1.865 kJ·kg^{-1}·K^{-1}).

For IEE at an applied voltage of 1.5 V, $T_1 = 343.65$ K, $T_0 = 295.65$ K, $\Delta h_{\text{vapor}} = 4.18 \cdot (373.15 - 343.65) + 2260 + 1.865 \cdot (343.65 - 373.15) = 2328.29$ kJ·kg^{-1}, and the apparent energy efficiency is calculated as:

$$\eta = \frac{51.04/3600 \cdot [4.18 \cdot (343.65 - 295.65) + 2328.29]}{56.95 + 0} = 62.96\%$$

For solar-operated IEE under 20 kW·m^{-2} illumination and an applied voltage of 1.5 V, $T_1 = 363.05$ K, $T_0 = 294.95$ K, $\Delta h_{\text{vapor}} = 4.18 \cdot (373.15 - 363.05) + 2260 + 1.865 \cdot (363.05 - 373.15) = 2283.38$ kJ·kg^{-1}, and the apparent energy efficiency is calculated as:

$$\eta = \frac{100.66/3600 \cdot [4.18 \cdot (363.05 - 294.95) + 2283.38]}{56.95 + 20} = 93.31\%$$

Using the above standardized calculation method, the apparent energy efficiencies of the IEE and solar-operated IEE are 62.96% and 93.31%, respectively. Among them, the calculation parameters of IEE are: Electrical input is 56.95 kW·m^{-2}, solar irradiation is 0 kW·m^{-2}, latent heat of the vaporization is 2328.29 kJ/kg^{-1}, and sensible heat of the vapor is 200.64 kJ/kg^{-1}. For the solar-operated IEE, the corresponding calculation parameters are: Electrical input is 56.95 kW·m^{-2}, solar irradiation is 20 kW·m^{-2}, latent heat of the vaporization is 2283.38 kJ/kg^{-1}, and sensible heat of the vapor is 284.66 kJ/kg^{-1}. Since the evaporation interface temperatures of the both evaporators are higher than the ambient temperature, there is no input contribution of environmental heat. All the results are summarized in Table 4-1.

Table 4-1. Calculation data of apparent energy efficiency

Sample	Evaporation rate (kg·m^{-2}·h^{-1})	Latent heat (kJ·kg^{-1})	Sensible heat (kJ·kg^{-1})	Electrical input (kW·m^{-2})	Solar irradiation input (kW·m^{-2})	Apparent energy efficiency (%)
IEE	51.04	2328.29	200.64	56.95	0	62.96
Solar-operated IEE	100.66	2283.38	284.66	56.95	20	93.31

The relatively high apparent energy efficiency of the solar-operated IEE arises from its 3D evaporation interface, which provides a larger effective evaporation area within its hierarchical porous structure.[6,7] This phenomenon has been widely reported in previous 3D photothermal evaporation studies, contributes directly to the high solar-to-vapor efficiency.[6,8,9] Importantly, the calculation method based on projected area is the universally accepted standard in the interfacial photothermal evaporation field, which ensures a direct comparison of performance between different evaporation systems with various structures and dimensions. Using this standardized metric, the solar-operated IEE also maintains excellent evaporation performance under real-world outdoor operating conditions.

Supplementary Note 5. Energy analysis of solar-operated IEE

We conducted an energy analysis for the solar-operated IEE, with the energy balance equation given as follows:

$$P_{\text{evaporation}} + P_{\text{opt}} + P_{\text{conduction}} + P_{\text{radiation}} + P_{\text{convection}} + P_{\text{wire}} = P_{\text{electricity}} + P_{\text{solar}}$$

The external input energy of solar-operated IEE includes electrical input ($P_{\text{electricity}}$) and solar irradiation input (P_{solar}). The energy budget of the system includes not only the evaporation energy ($P_{\text{evaporation}}$) utilized by solar-operated IEE, but also various losses such as optical loss (P_{opt}), apparent heat conduction loss ($P_{\text{conduction}}$), apparent heat radiation loss ($P_{\text{radiation}}$), apparent heat convection loss ($P_{\text{convection}}$), and Joule heat loss in the connecting wires (P_{wire}).

The $P_{\text{electricity}}$ of the solar-operated IEE is 56.95 kW·m^{-2}, and the P_{solar} of the solar-operated IEE is 20 kW·m^{-2}. The latent heat of vaporization is calculated as follow:

$$\begin{aligned}\Delta h_{\text{vapor}} &= C_{\text{liquid}} \cdot (373.15 - T_1) + \Delta h_{100} + C_{\text{vapor}} \cdot (T_1 - 373.15) \\ &= 4.18 \cdot (373.15 - 363.05) + 2260 + 1.865 \cdot (363.05 - 373.15) \\ &= 2283.38\ \text{kJ} \cdot \text{kg}^{-1}\end{aligned}$$

where Δh_{vapor} is latent heat of vaporization (kJ·kg^{-1}), C_{liquid} is specific heat capacity of water (4.18 kJ·kg^{-1}·K^{-1}), T_1 is the steady-state temperature of the evaporation interface (K), Δh_{100} is the latent heat of water at 100 °C (373.15 K, taken to be 2260 kJ·kg^{-1}), and the C_{vapor} is the specific heat capacity of vapor (1.865 kJ·kg^{-1}·K^{-1}).

Further, the calculation formula of $P_{\text{evaporation}}$ is as follows:

$$\begin{aligned}P_{\text{evaporation}} &= \dot{m} \cdot \left[C_{\text{liquid}} \cdot (T_1 - T_0) + \Delta h_{\text{vapor}}\right] \\ &= \frac{100.66}{3600} \cdot [4.18 \cdot (363.05 - 294.95) + 2283.38] = 71.81\ \text{kW} \cdot \text{m}^{-2}\end{aligned}$$

where $\dot{m}$ is evaporation rate (kg·m^{-2}·h^{-1}), C_{liquid} is specific heat capacity of water (4.18 kJ·kg^{-1}·K^{-1}), T_1 is the steady-state temperature of the evaporation interface (K), T_0 is the initial temperature of the evaporation interface (K), Δh_{vapor} is latent heat of vaporization

(kJ·kg^{-1}), Among them, $C_{\text{liquid}} \cdot (T_1 - T_0)$ is the sensible heat of vapor, $\dot{m} \cdot C_{\text{liquid}} \cdot (T_1 - T_0)$ is the utilization of sensible heat, and $\dot{m} \cdot \Delta h_{\text{vapor}}$ is the utilization of latent heat.

The calculation formula of P_{opt} is as follows:

$$P_{\text{opt}} = P_{\text{solar}}(1 - \alpha) = 20 \cdot (100 - 98.29)/100 = 0.34\ \text{kW} \cdot \text{m}^{-2}$$

where P_{solar} is input of solar energy (kW·m^{-2}), and α is the solar absorption of IEE.

The calculation formula of $P_{\text{conduction}}$ is as follows:

$$P_{\text{conduction}} = \frac{cm\Delta T}{hS_1} = \frac{4.18 \cdot 92.30 \cdot 1.6}{3600 \cdot 0.0018 \cdot 1000} = 0.10\ \text{kW} \cdot \text{m}^{-2}$$

where c is the specific heat capacity of liquid water (J·g^{-1}·K^{-1}), m is the mass of the bulk brine (g), ΔT is the temperature change of the bulk brine (K), $\Delta T = T_3 - T_2$, T_3 is the temperature of the bulk brine when the solar evaporator is stably evaporating (K), T_2 is the initial temperature of the bulk brine (K), h is the test time (s), and S_1 is the projection area of the test container (m^2).

The calculation formula of $P_{\text{radiation}}$ is as follows:

$$P_{\text{radiation}} = \epsilon\sigma\left({T_{\text{top}}}^4 - {T_{\text{m}}}^4\right) = 1 \cdot 5.67 \cdot 10^{-8} \cdot (363.05^4 - 299.75^4)/1000$$
$$= 0.53\ \text{kW} \cdot \text{m}^{-2}$$

where ϵ is the emissivity of the solar evaporator, σ is the Stefan-Boltzmann constant (5.67×10^{-8} W·m^{-2}·K^{-4}), T_{top} is the average temperature of the evaporation interface during the stable evaporation of the solar evaporator (K), T_{m} is the ambient temperature (K).

The calculation formula of $P_{\text{convection}}$ is as follows:

$$P_{\text{convection}} = h_0\left(T_{\text{top}} - T_{\text{m}}\right) = 5 \cdot (363.05 - 299.75)/1000 = 0.32\ \text{kW} \cdot \text{m}^{-2}$$

where h_0 is the convective heat transfer coefficient (5 W·m^{-2}·K^{-1}), T_{top} is the average temperature of the evaporation interface when the solar evaporator is stably evaporated (K), T_{m} is the ambient temperature (K).

The calculation formula of P_{wire} is as follows:

$$P_{\text{wire}} = \frac{I^2 R}{S_2} = \frac{9.72^2 \cdot 0.048}{0.002 \cdot 1000} = 2.27\ \text{kW} \cdot \text{m}^{-2}$$

where I is the input current (A), R is the resistance of the wire (Ω), and S_2 is the projection area of the wire (m^2).

The calculation parameters of IEE are as follows: electrical input, 56.95 $kW \cdot m^{-2}$; solar irradiation, 20 $kW \cdot m^{-2}$; optical loss, 0.34 $kW \cdot m^{-2}$; apparent heat conduction loss, 0.10 $kW \cdot m^{-2}$; apparent heat radiation loss, 0.53 $kW \cdot m^{-2}$; apparent heat convection loss, 0.32 $kW \cdot m^{-2}$; and Joule heat loss in wires, 2.27 $kW \cdot m^{-2}$. All calculations are performed with values rounded to two decimal places. The results are summarized in Table 5-1.

Table 5-1. Calculation data of energy input and energy output for solar-operated IEE

Electrical input ($kW \cdot m^{-2}$)	Solar irradiation input ($kW \cdot m^{-2}$)	Evaporation ($kW \cdot m^{-2}$)	Optical loss ($kW \cdot m^{-2}$)	Apparent heat conduction loss ($kW \cdot m^{-2}$)	Apparent heat radiation loss ($kW \cdot m^{-2}$)	Apparent heat convection loss ($kW \cdot m^{-2}$)	Joule heat loss in wires ($kW \cdot m^{-2}$)
56.95	20	71.81	0.34	0.10	0.53	0.32	2.27

The energy input of the solar-operated IEE, comprising electrical input and solar irradiation, is quantified at 76.95 $kW \cdot m^{-2}$. Correspondingly, the energy output of the solar-operated IEE including evaporation, optical loss, heat conduction loss, heat radiation loss, heat convection loss, and Joule heat loss in wires, is 75.37 $kW \cdot m^{-2}$. The calculated results of solar-operated IEE exhibit remarkable consistency between energy input and output within the experimental error range. Furthermore, the closed energy balance clearly demonstrates that the reported ultrahigh evaporation rate of solar-operated IEE is fully sustainable under the specified operating conditions.

Supplementary Note 6. Calculation of energy utilization efficiency of solar-operated IEE

The energy budget of the system includes not only the evaporation energy ($Q_{\mathrm{evaporation}}$) utilized by solar-operated IEE, but also various losses such as optical loss (Q_{opt}), heat conduction loss ($Q_{\mathrm{conduction}}$), heat radiation loss ($Q_{\mathrm{radiation}}$), heat convection loss ($Q_{\mathrm{convection}}$), and Joule heat loss in the connecting wires (Q_{wire}). The energy balance equation for the IEE in the photothermal-electrothermal co-evaporation can be expressed as:

$$Q_{\mathrm{evaporation}} + Q_{\mathrm{opt}} + Q_{\mathrm{conduction}} + Q_{\mathrm{radiation}} + Q_{\mathrm{convection}} + Q_{\mathrm{wire}} = Q_{\mathrm{solar}} + Q_{\mathrm{electricity}}$$

The heat loss is deducted from the total input energy to derive the effective energy utilized for water evaporation, thereby enabling the calculation of the corresponding energy utilization efficiency (η).

$$\eta = \frac{Q_{\mathrm{solar}} + Q_{\mathrm{electricity}} - Q_{\mathrm{opt}} - Q_{\mathrm{conduction}} - Q_{\mathrm{radiation}} - Q_{\mathrm{convection}} - Q_{\mathrm{wire}}}{Q_{\mathrm{electricity}} + Q_{\mathrm{solar}}}$$

The $Q_{\mathrm{electricity}}$ is 14.58 W, and the calculation formula of Q_{solar} is as follows:

$$Q_{\mathrm{solar}} = P_{\mathrm{solar}} \cdot S_{\mathrm{proj}} = 20000 \cdot 0.000256 = 5.12\ \mathrm{W}$$

where P_{solar} is power density of solar energy ($\mathrm{W \cdot m^{-2}}$), and S_{proj} is the top projected area of IEE ($\mathrm{m^2}$).

The calculation formula of Q_{opt} is as follows:[10]

$$Q_{\mathrm{opt}} = Q_{\mathrm{solar}}(1 - \alpha) = 5.12 \cdot (1 - 0.9829) = 0.09\ \mathrm{W}$$

where Q_{solar} is input of solar energy (W), and α is the solar absorption of IEE.

The calculation formula of $Q_{\mathrm{conduction}}$ is as follows:[10]

$$Q_{\mathrm{conduction}} = \frac{cm\Delta T}{h} = 4.18 \cdot 92.30 \cdot 1.6/3600 = 0.17\ \mathrm{W}$$

where c is the specific heat capacity of liquid water ($\mathrm{J \cdot g^{-1} \cdot K^{-1}}$), m is the mass of the bulk brine (g), ΔT is the temperature change of the bulk brine (K), $\Delta T = T_3 - T_2$, T_3 is the temperature of the bulk brine when the solar evaporator is stably evaporating (K), T_2 is the initial temperature of the bulk brine (K), and h is the test time (s).

The calculation formula of $Q_{\mathrm{radiation}}$ is as follows:[10]

$$Q_{\text{radiation}} = \epsilon\sigma\left[\left(T_{\text{top}}{}^4 - T_{\text{m}}{}^4\right)\cdot S_{\text{proj}} + \left(T_{\text{lateral}}{}^4 - T_{\text{m}}{}^4\right)\cdot S_{\text{lateral}}\right]$$
$$= 1\cdot 5.67\cdot 10^{-8}\cdot\begin{bmatrix}(363.05^4 - 299.75^4)\cdot 0.000256\\ +(354.75^4 - 299.75^4)\cdot 0.000384\end{bmatrix} = 0.30\ \text{W}$$

where ϵ is the emissivity of the solar evaporator, σ is the Stefan-Boltzmann constant (5.67×10^{-8} W·m^{-2}·K^{-4}), T_{top} is the average temperature of the top evaporation interface during the stable evaporation of the solar evaporator (K), T_{lateral} is the average temperature of the lateral evaporation interface during the stable evaporation of the solar evaporator (K), T_{m} is the ambient temperature (K), S_{proj} is the top projected area of IEE (m^2), and S_{lateral} is the lateral area of IEE (m^2).

The calculation formula of $Q_{\text{convection}}$ is as follows:[10]

$$Q_{\text{convection}} = h_0\left[\left(T_{\text{top}} - T_{\text{m}}\right)\cdot S_{\text{proj}} + \left(T_{\text{lateral}} - T_{\text{m}}\right)\cdot S_{\text{lateral}}\right]$$
$$= 5\cdot\begin{bmatrix}(363.05 - 299.75)\cdot 0.000256\\ +(354.75 - 299.75)\cdot 0.000384\end{bmatrix} = 0.19\ \text{W}$$

where h_0 is the convective heat transfer coefficient (5 W·m^{-2}·K^{-1}), T_{top} is the average temperature of the evaporation interface when the solar evaporator is stably evaporated (K), T_{lateral} is the average temperature of the lateral evaporation interface during the stable evaporation of the solar evaporator (K), T_{m} is the ambient temperature (K), S_{proj} is the top projected area of IEE (m^2), and S_{lateral} is the lateral area of IEE (m^2).

The calculation formula of Q_{wire} is as follows:

$$Q_{\text{wire}} = I^2R = 9.72^2\cdot 0.048 = 4.53\ \text{W}$$

where I is the input current and R is the resistance of the wire (Ω).

The calculation of η is as follows:

$$\eta = \frac{Q_{\text{solar}} + Q_{\text{electricity}} - Q_{\text{opt}} - Q_{\text{conduction}} - Q_{\text{radiation}} - Q_{\text{convection}} - Q_{\text{wire}}}{Q_{\text{electricity}} + Q_{\text{solar}}}$$
$$= \frac{5.12 + 14.58 - 0.09 - 0.17 - 0.30 - 0.19 - 4.53}{5.12 + 14.58} = 73.20\%$$

Using the above calculation formula, the actual energy utilization efficiency of the solar-operated IEE is calculated to be 73.20%, far exceeding the <20% efficiency of conventional electrothermal evaporators, demonstrating the superior heat utilization capability of the solar-operated IEE. The calculation parameters of IEE are as follows: electrical input, 14.58 W; solar

irradiation, 5.12 W; optical loss, 0.09 W; heat conduction loss, 0.17 W; heat radiation loss, 0.30 W; heat convection loss, 0.19 W; and Joule heat loss in wires, 4.53 W. The results are summarized in Table 6-1.

Table 6-1. Calculation data of energy utilization efficiency

Sample	Optical loss (W)	Heat conduction loss (W)	Heat radiation loss (W)	Heat convection loss (W)	Joule heat loss in wires (W)	Electrical input (W)	Solar irradiation (W)	Energy utilization efficiency (%)
Solar-operated IEE	0.09	0.17	0.3	0.19	4.53	14.58	5.12	73.20

Supplementary Note 7. Theoretical calculation

In this project, the current, laminar flow, heat transfer, and water transport modules in COMSOL are used for coupling calculation respectively.

The current model is solved based on the following equations:

$$\nabla \cdot J = Q_{\mathrm{j,v}}$$

$$J = \sigma E + \frac{\partial D}{\partial t} + J_{\mathrm{e}}$$

$$E = -\nabla v$$

where J is the current density, $Q_{\mathrm{j,v}}$ is the volume charge density, σ represents the conductivity of the material, E represents the electric field strength, D is the electric displacement field, t is the time, J_{e} is the extra current source term, and v is the electric potential.

Laminar flow module:

$$\rho \frac{\partial u}{\partial t} + \rho(u \cdot \nabla)u = \nabla \cdot [-pI + \mu(\nabla u + (\nabla u)^T] + F + \rho g$$

where ρ is the material density, u is the space fluid velocity field, t is the time, p is the fluid pressure, I is the unit tensor matrix, F is the applied volume force, T represents the transpose, the transpose operation is performed on the velocity gradient tensor, g is the gravitational acceleration, and μ is the dynamic viscosity.

Heat transfer module:

$$\rho C_{\mathrm{p}} \frac{\partial T}{\partial t} + \rho C_{\mathrm{p}} u \cdot \nabla T + \nabla \cdot q = Q + Q_{\mathrm{p}} + Q_{\mathrm{vd}}$$

$$q = -k\nabla T$$

where ρ is the material density, C_{p} is material specific heat capacity, u is space fluid velocity field, T is temperature, t is the time, q is heat flux, Q is generalized heat source power, Q_{p} is phase change heat source power, Q_{vd} is water vapor condensation heat source power, k is material thermal conductivity.

Moisture transport module:

$$M_{\mathrm{v}}\frac{\partial C_{\mathrm{v}}}{\partial t} + M_{\mathrm{v}}u \cdot \nabla c_{\mathrm{v}} + \nabla \cdot g_{\mathrm{w}} = G$$

$$C_{\mathrm{v}} = \emptyset_{\mathrm{w}} C_{\mathrm{sat}}$$

where M_{v} is the molar mass of water, $\frac{\partial c_{\mathrm{v}}}{\partial t}$ is the change rate of water vapor concentration with time, u is the spatial fluid velocity field, c_{v} is the vapor concentration, g_{w} is the water vapor flux, G is the water vapor source, $\emptyset_{\mathrm{w}}$ is the relative humidity, C_{sat} is the saturated concentration of water vapor.

Supplementary Note 8. Calculation of rejection

The calculation formula is presented below:[11,12]

$$R = \frac{C_{\mathrm{i}} - C_{\mathrm{f}}}{C_{\mathrm{i}}} \cdot 100\%$$

where R is the rejection (%), C_{i} is the initial ion concentration of Bohai seawater (mg·L^{-1}), and C_{f} is the ion concentration of produced freshwater (mg·L^{-1}).

Supplementary Note 9. Measurement of salt transport flux

In the salt transport flux measurement process, the salt was first spread evenly on the EI.[13,14] Meanwhile, the IEE was dry, the salt transport area is S, and the salinity of the bulk brine is C_1. When the IEE comes into contact with the brine, start the timer. During time t, the salt at the EI of the IEE continuously transfers salt into the bulk brine due to salt gradients and gravity. At this time, the mass of the bulk brine is m, and the salinity of the bulk brine is C_2. Therefore, the formula for calculating the salt transport flux (J) of the IEE is as follows:

$$J = \frac{m(C_2 - C_1)}{S \cdot \mathrm{t}}$$

In this measurement, C_1=3.5 wt% and t= 5 min.

Supplementary Note 10. Measurement of water transport rate

The IEE was placed vertically in 3.5 wt% NaCl solution, and a piece of dust-free paper was attached to its top EI.[15,16] The height of the evaporator above the brine is 1.8 cm. The water transport rate was calculated by the following formula:

$$W = \frac{H}{t}$$

where W is the water transport rate ($cm \cdot s^{-1}$), H is the height of the IEE above the brine (cm), and t is the wetting time of the dust-free paper at the EI (s).

Supplementary Note 11. Outdoor experiments of solar-operated IEE

The Fresnel lens converges natural light into high-intensity illumination and irradiates the evaporation interface of the IEE. Meanwhile, the solar cells convert solar energy into electrical energy, which is transmitted to the IEE through connecting wires. When the Fresnel lens and solar cell were integrated to IEE, the synergistic energy supply of solar energy and electrical energy was realized. In terms of solar energy utilization, the concentrated light intensity by the lens fluctuates to a certain extent owing to the variation in natural light intensity. Nevertheless, the overall average light intensity remains approximately 20 $kW \cdot m^{-2}$, with the specific parameters presented in Supplementary Table 6. In terms of electric power supply, the operating voltage of a single IEE is 1.5 V, and the total voltage required for twelve integrated IEEs is 18 V. Accordingly, the solar cells with a combined output voltage exceeding 18 V, were adopted to ensure the stable and continuous operation of the IEE outdoors.

Supplementary Note 12. Analysis of freshwater production process.

The vapor-to-water efficiency ($\eta_{\mathrm{V-W}}$) is calculated by the following formula:

$$\eta_{\mathrm{V-W}} = \frac{F \cdot \rho}{\dot{m}} = \frac{66.72 \cdot 1}{107.80} = 61.89\%$$

where F is the freshwater flux (L·m^{-2}·h^{-1}), ρ is the density of water (1 kg·L^{-1}), and $\dot{m}$ is evaporation rate (kg·m^{-2}·h^{-1}). Without customized condensation structures for freshwater harvesting, this vapor-to-water efficiency of 61.89% is comparable to the performance reported in most literature.[17,18] And we also calculated the condensation power ($P_{\mathrm{condensation}}$) of the system.[19] The condensation power is defined as the thermal power corresponding to latent heat released by vapor phase change at the condensation interface, and can be determined by multiplying the freshwater by the latent heat of vaporization. Among them, the latent heat of vaporization is calculated as follow:

$$\begin{aligned}\Delta h_{\mathrm{vapor}} &= C_{\mathrm{liquid}} \cdot (373.15 - T_1) + \Delta h_{100} + C_{\mathrm{vapor}} \cdot (T_1 - 373.15) \\ &= 4.18 \cdot (373.15 - 363.05) + 2260 + 1.865 \cdot (363.05 - 373.15) \\ &= 2283.38\ \mathrm{kJ \cdot kg^{-1}}\end{aligned}$$

where $\Delta h_{\mathrm{vapor}}$ is latent heat of vaporization (kJ·kg^{-1}), C_{liquid} is specific heat capacity of water (4.18 kJ·kg^{-1}·K^{-1}), T_1 is the steady-state temperature of the evaporation interface (K), Δh_{100} is the latent heat of water at 100 °C (373.15 K, taken to be 2260 kJ·kg^{-1}), and the C_{vapor} is the specific heat capacity of vapor (1.865 kJ·kg^{-1}·K^{-1}).

Accordingly, $P_{\mathrm{condensatio}} = F \cdot \rho \cdot \Delta h_{\mathrm{vapor}} = 66.72 \cdot 1 \cdot \frac{2283.38}{3600} = 42.32\ \mathrm{kW \cdot m^{-2}}$

where F is freshwater flux (L·m^{-2}·h^{-1}), ρ is the density of water (1 kg·L^{-1}), and $\Delta h_{\mathrm{vapor}}$ is latent heat of vaporization (kJ·kg^{-1}). The total freshwater production efficiency (η_{TFP}) is defined as the heat of condensation compared to total energy input, which is calculated according to the following formula:[20]

$$\eta_{\mathrm{TFP}} = \frac{P_{\mathrm{condensation}}}{P_{\mathrm{solar}} + P_{\mathrm{electricity}}} = \frac{42.32}{20 + 56.95} = 55\%$$

The total freshwater production efficiency of 55% is close to the evaporation-condensation devices reported in the literature, confirming the rationality of ultrahigh evaporation rates directly translate to high freshwater flux.[21,22]

In addition, we used a hygrometer to monitor internal humidity variations during the process of freshwater production. The results show that humidity increases gradually with continued evaporation and eventually stabilizes at approximately 89 % relative humidity (RH), which is significantly below the saturation level of 100 %RH (Figure 12-1). This observation demonstrates the establishment of a dynamic equilibrium between evaporation and condensation within the evaporation-condensation configuration, enabling steady and continuous freshwater production.

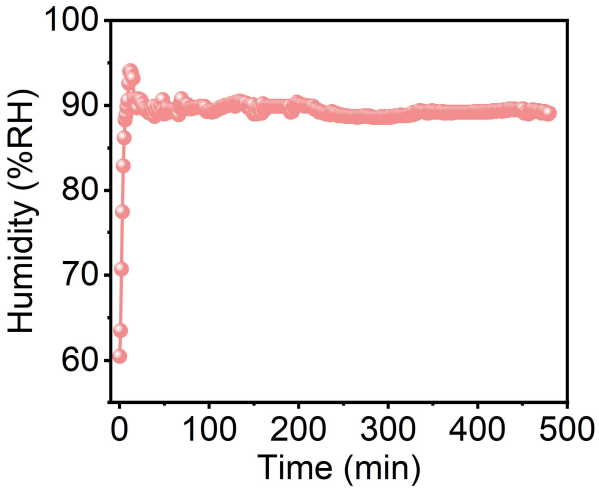
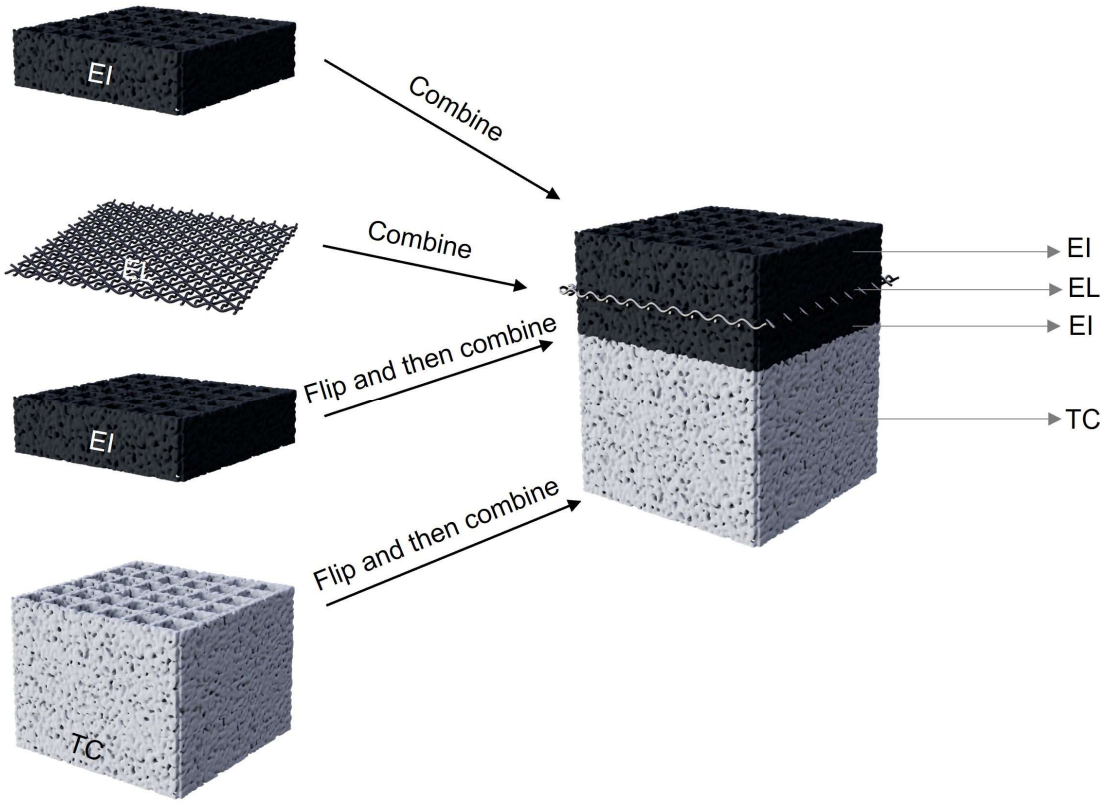
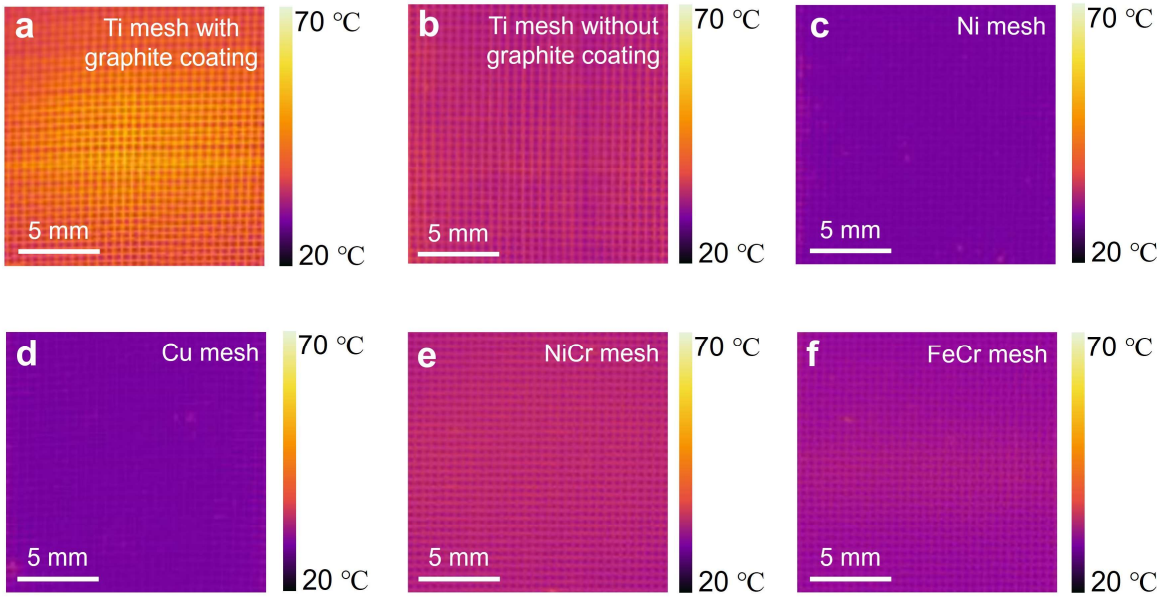


Figure 12-1. Humidity changes within the evaporation-condensation configuration.

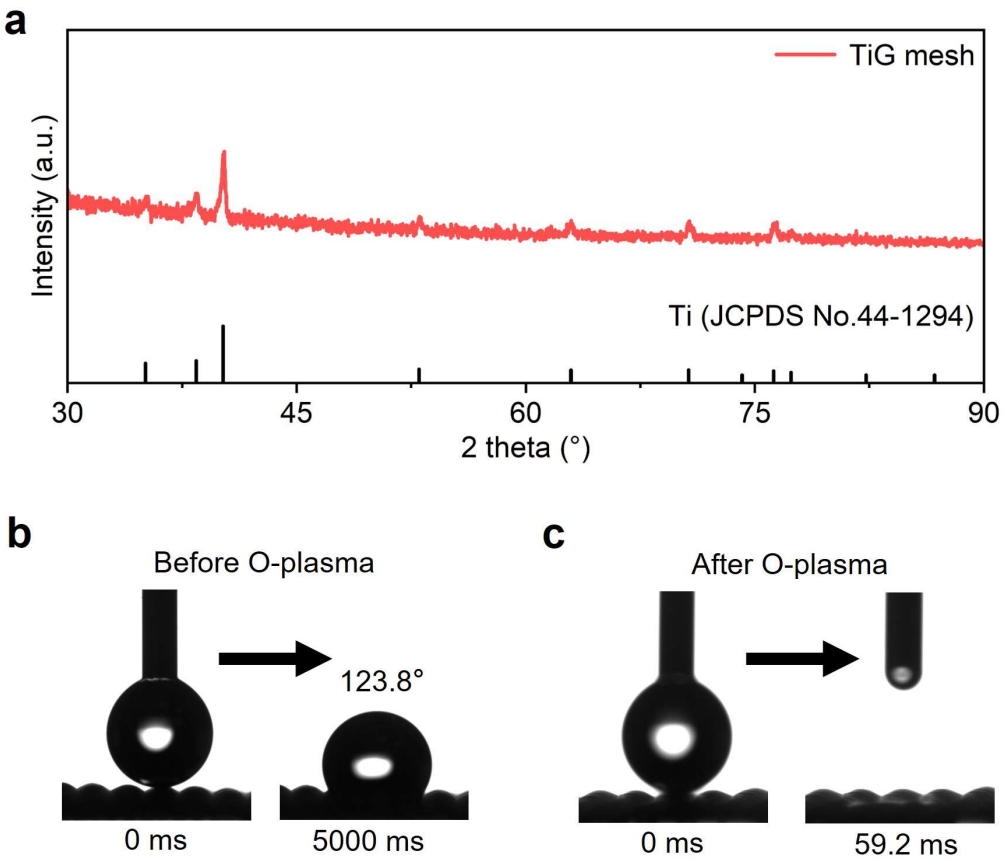
Supplementary Figures



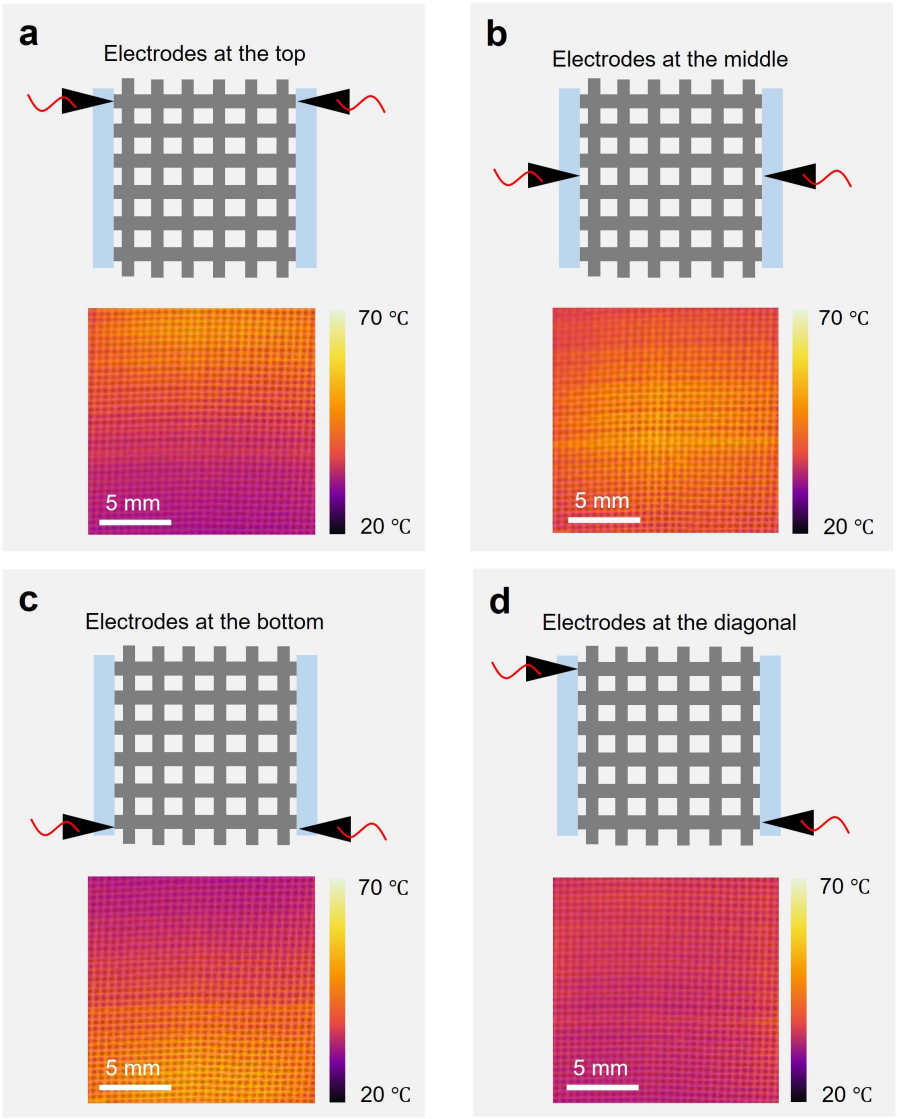
Supplementary Figure 1. Schematic of the IEE composed of different components.



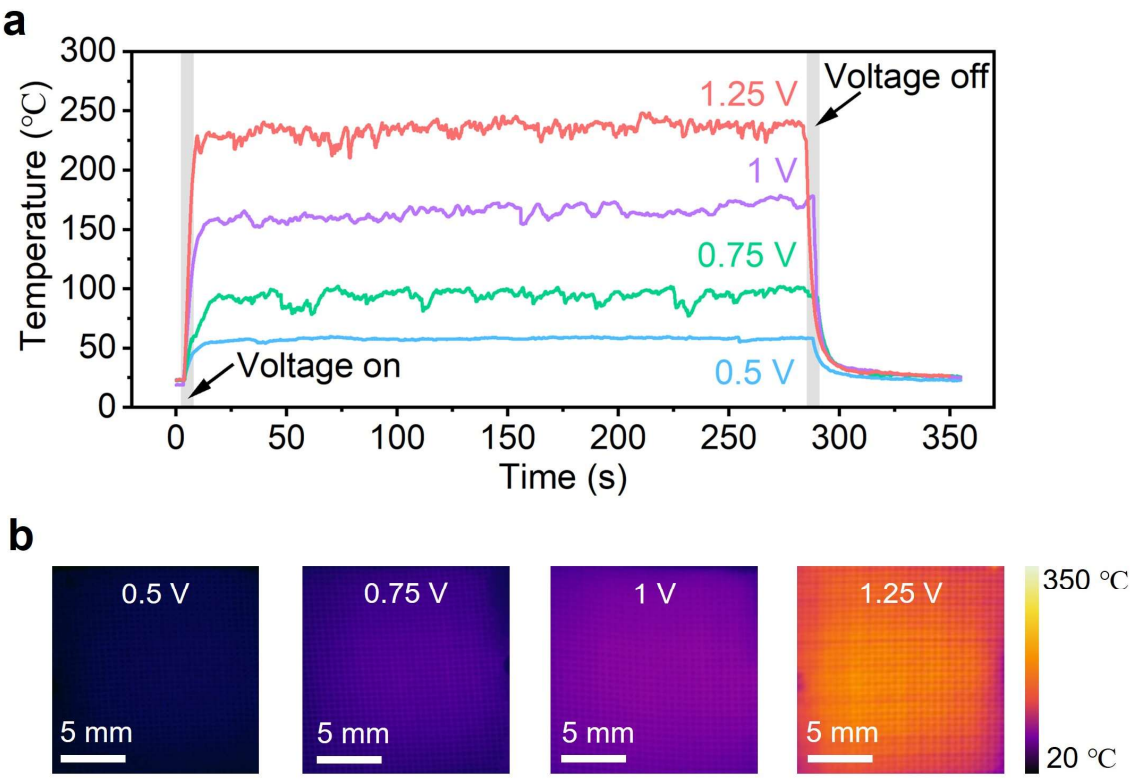
Supplementary Figure 2. Infrared thermal images of different metal meshes at 0.5 V.



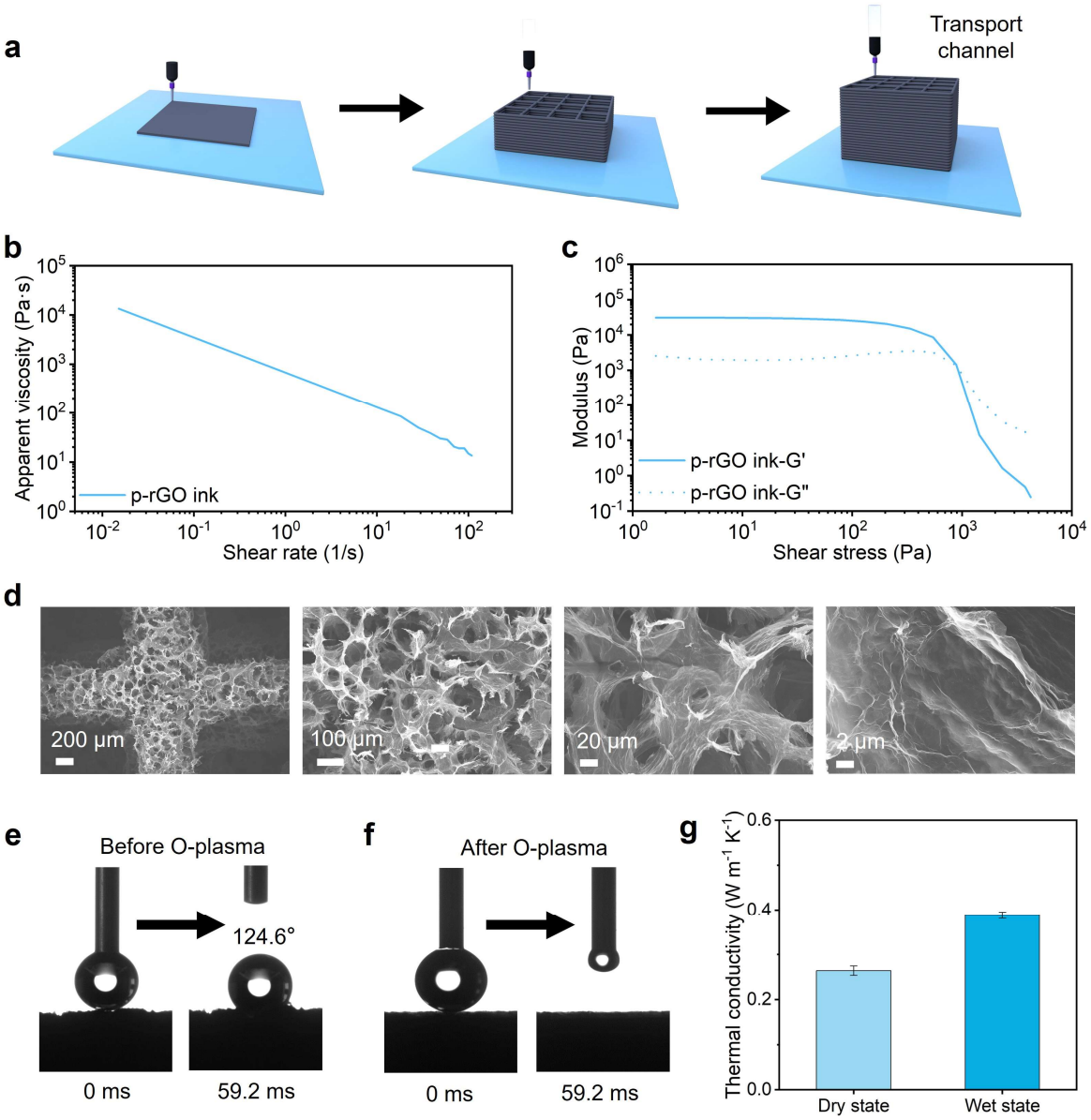
Supplementary Figure 3. Characterization of the TiG mesh. (a) XRD pattern of TiG mesh. Water contact angle of the TiG mesh (b) before and (c) after O-plasma treatment.



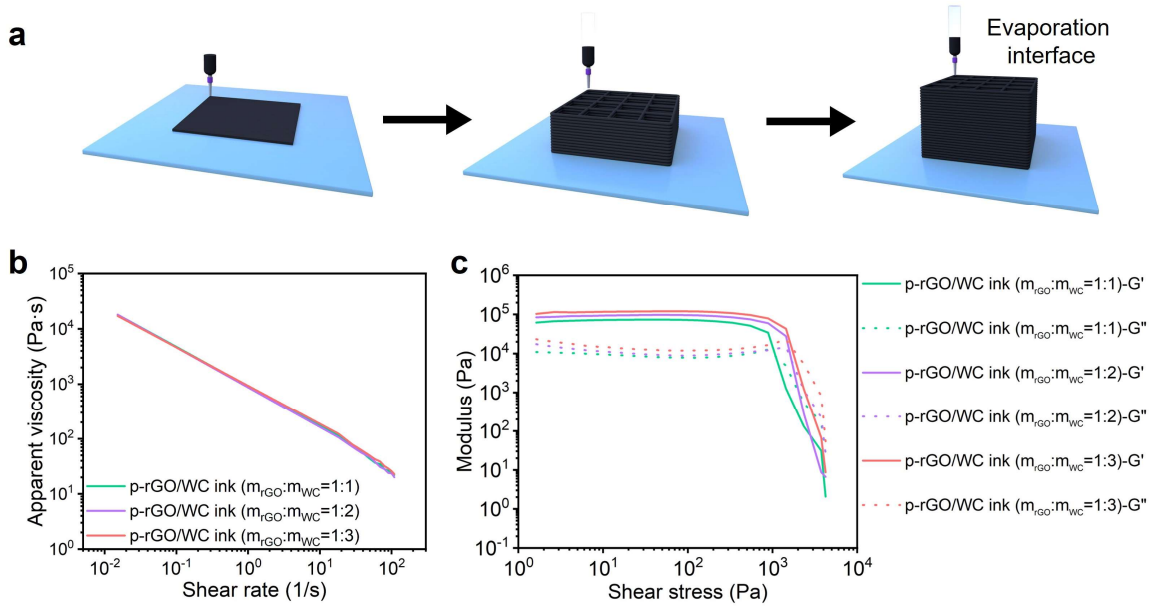
Supplementary Figure 4. Infrared thermal images of the TiG mesh with electrode (a) at the top, (b) at the middle, (c) at the bottom, and (d) at the diagonal with voltage of 0.5 V.



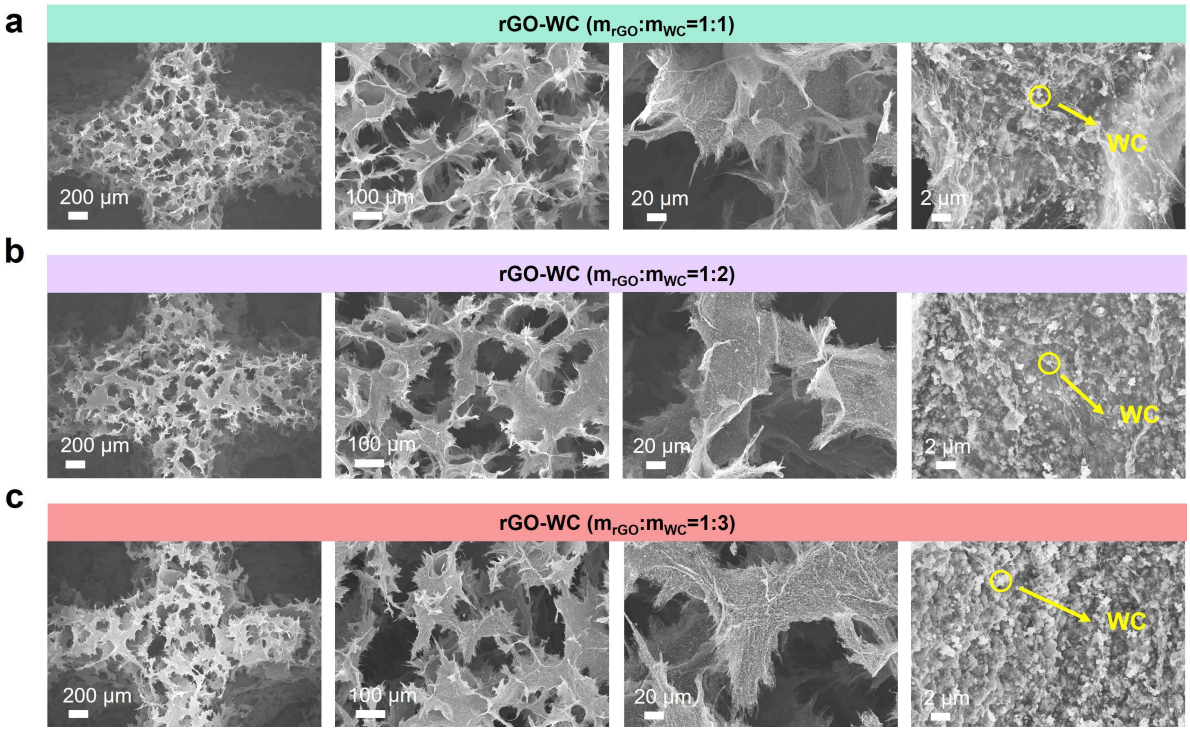
Supplementary Figure 5. Electrothermal properties of TiG mesh. (a) Temperature changes of the TiG mesh under different input voltages. (b) Infrared images of the TiG mesh under different input voltages.



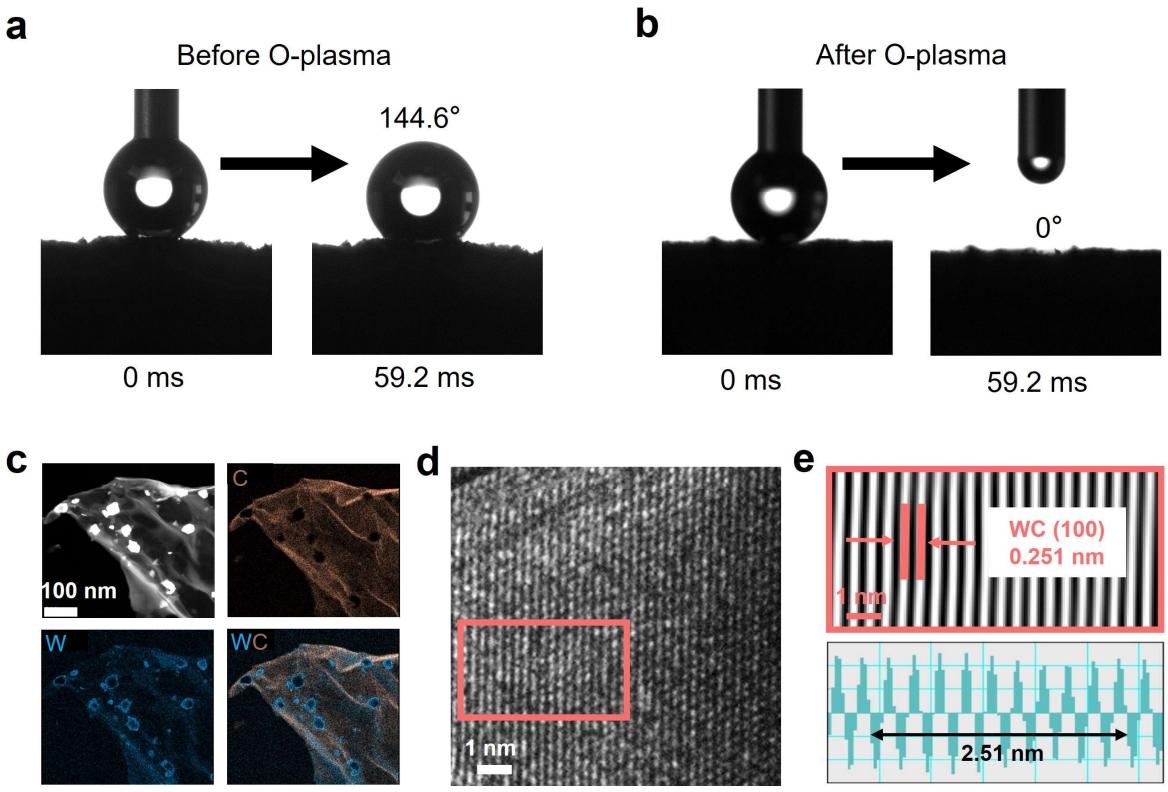
Supplementary Figure 6. Fabrication and characterization of the rGO TC. (a) Schematic of the 3D-printed TC using the p-rGO ink. (b) Apparent viscosity as a function of shear rate for the p-rGO ink. (c) Storage modulus (G′) and loss modulus (G″) as a function of shear stress for the p-rGO ink. (d) SEM images of the rGO TC at different magnifications. Water contact angle of the rGO TC (e) before and (f) after O-plasma treatment. (g) Thermal conductivity of the rGO TC. The data represent mean values ± SD (n = 3 independent experimental replicates).



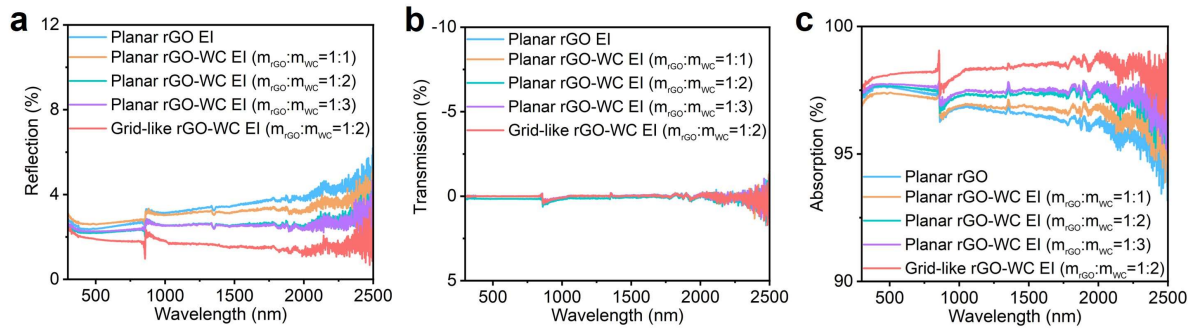
Supplementary Figure 7. Fabrication of the rGO-WC EI. (a) Schematic of the 3D-printed EI using the p-rGO/WC ink. (b) Apparent viscosity as a function of shear rate for the p-rGO/WC ink with different WC NPs ratios. (c) Storage modulus (G′) and loss modulus (G″) as a function of shear stress for the p-rGO/WC ink with different WC NPs ratios.



Supplementary Figure 8. Morphology of the rGO-WC EI. (a-c) SEM images of the rGO-WC with different WC NPs ratios at different magnifications.

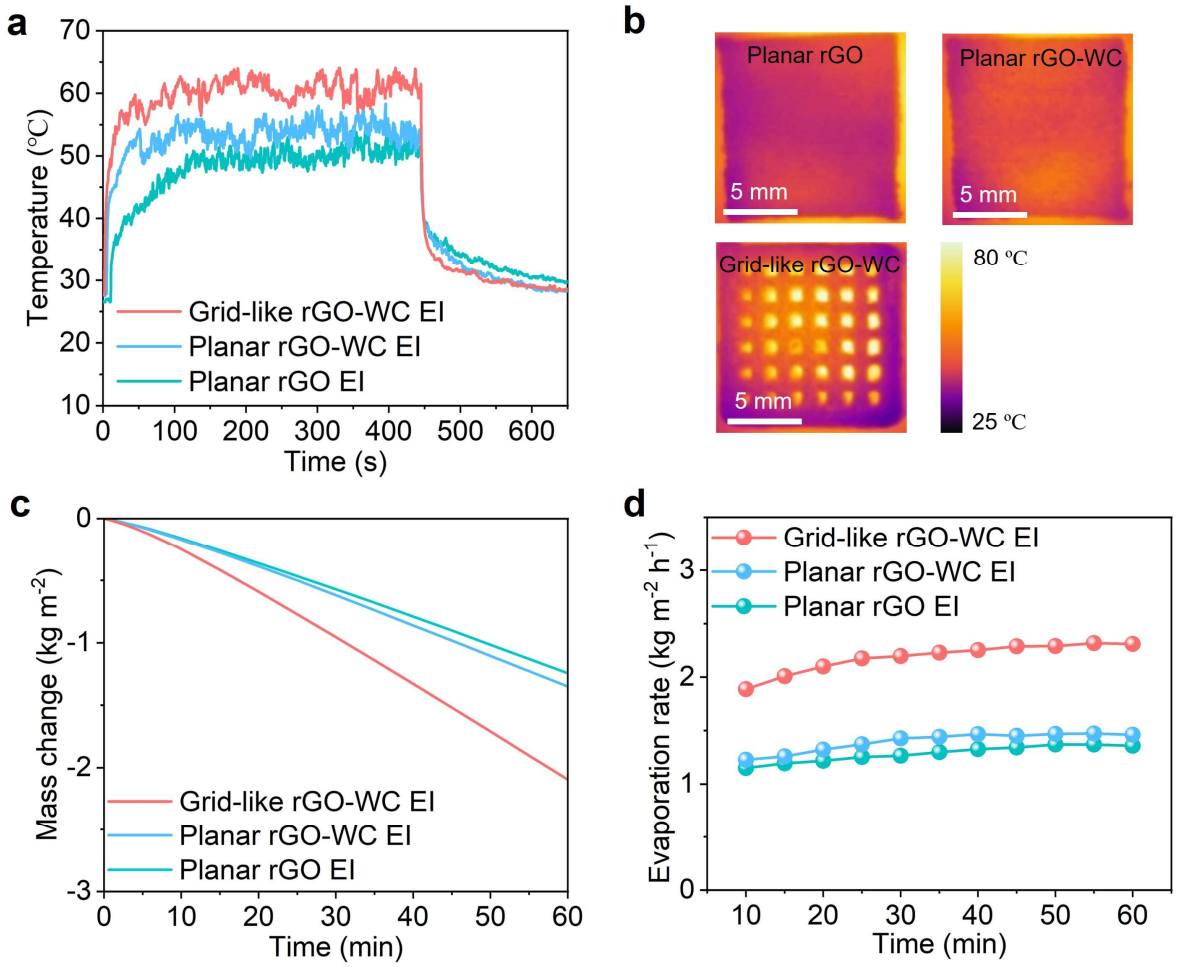


Supplementary Figure 9. Characterization of the rGO-WC EI. Water contact angle of the rGO-WC EI (a) before and (b) after O-plasma treatment. (c) TEM-EDX elemental mapping images of the rGO-WC EI. (d) Lattice fringe of the WC NPs in the rGO-WC EI. (e) IFFT image corresponding to the red box in (d) and line profile.



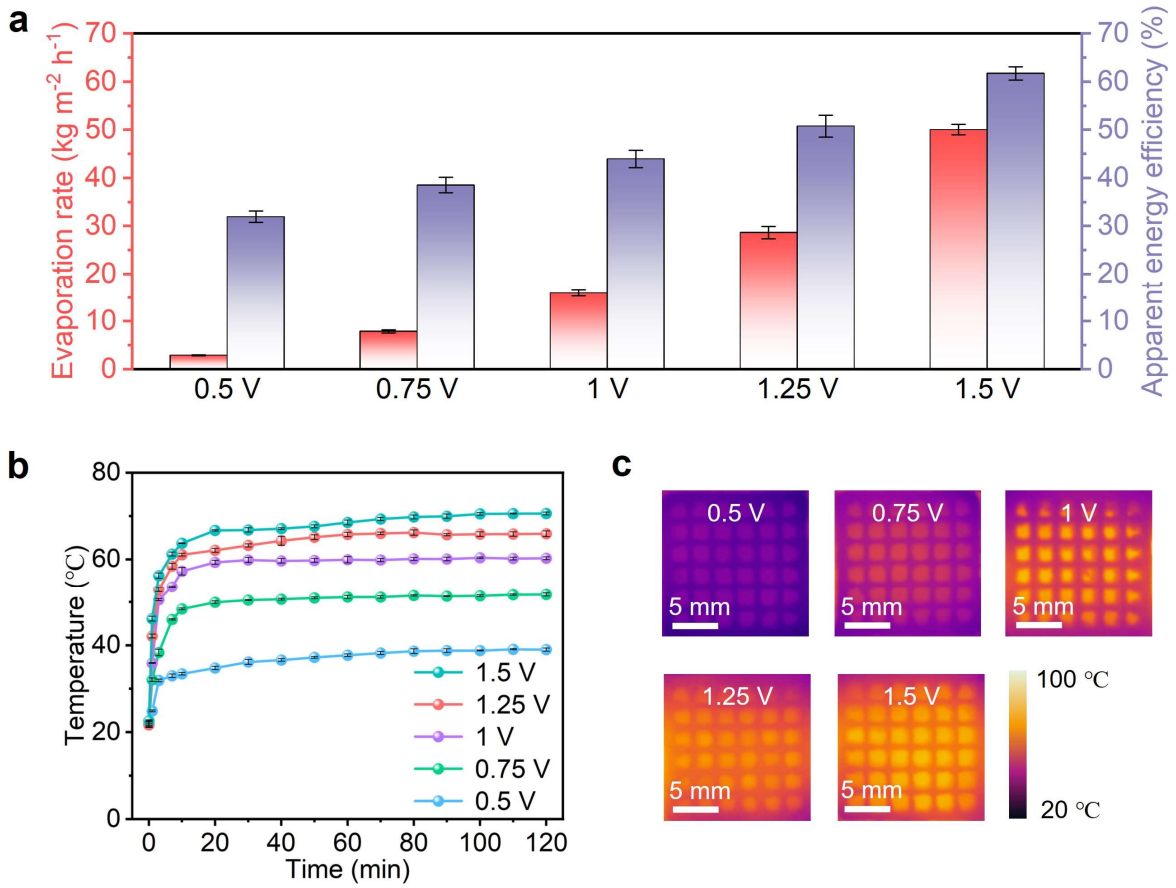
Supplementary Figure 10. Absorption of the rGO-WC EI. (a) Reflection spectra, (b) transmission spectra, and (c) absorption spectra of the planar rGO-WC EI with different WC NPs contents and grid-like rGO-WC EI at dry state.

With the increase in WC NPs content, the solar absorption of planar rGO-WC increased, and the solar absorption reached the equilibrium point of 96.82% at a ratio of rGO to WC NPs of 1:2. The grid-like rGO-WC EI further enhances solar absorption to 98.29%, attributable to the localized surface plasmon resonance effect of WC NPs and the antireflection properties of the 3D macrostructure.

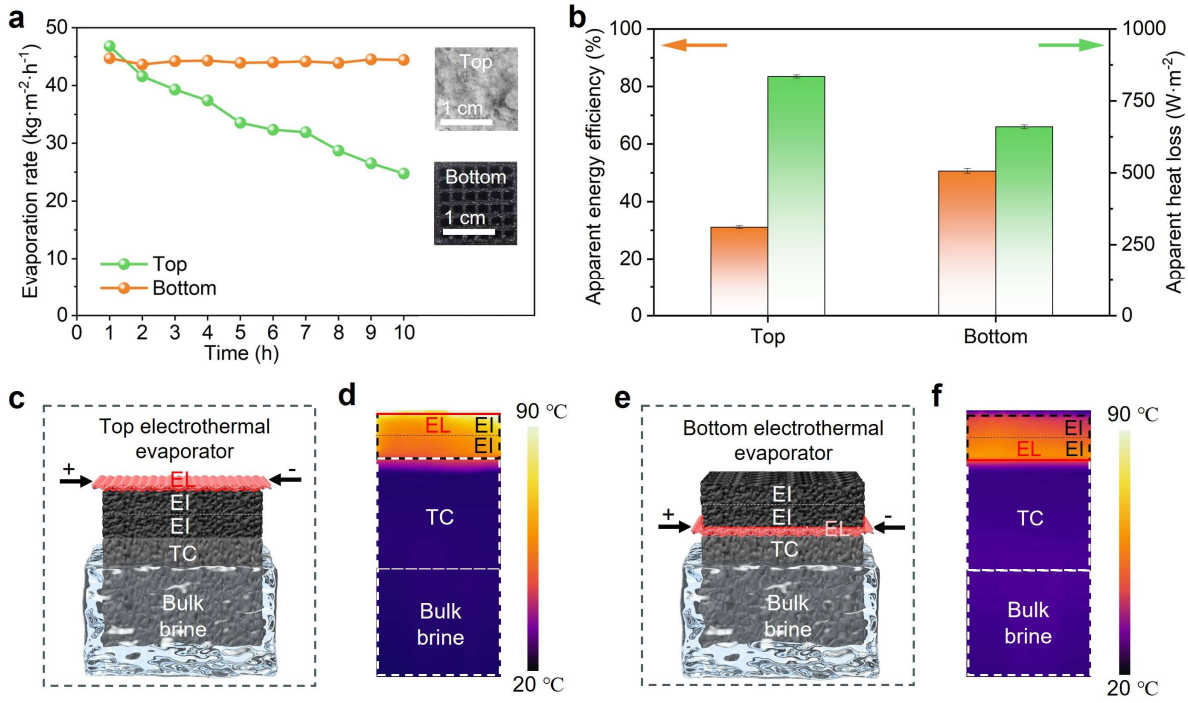


Supplementary Figure 11. Photothermal properties of rGO-WC EI. (a) Temperature changes and (b) infrared thermal images of the grid-like rGO-WC EI, the planar rGO-WC EI, and the planar rGO EI under 1 kW·m^{-2} illumination. (c) Mass changes and (d) evaporation rates of the photothermal evaporator with different EI.

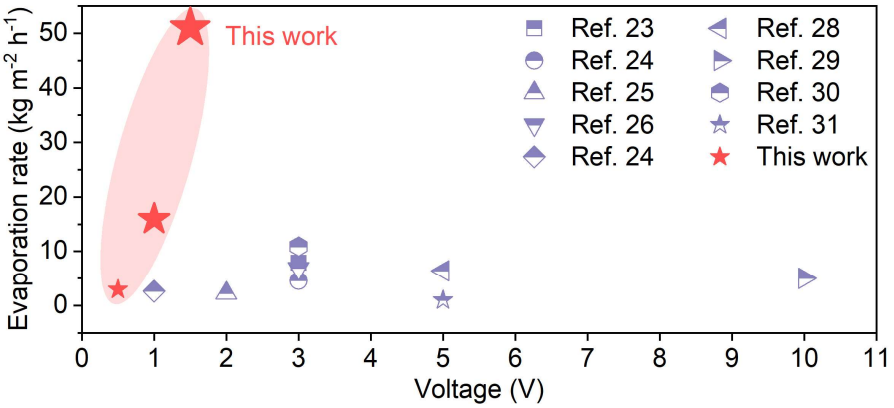
High solar absorption enables the generation of elevated surface temperatures, and the grid-like rGO-WC EI achieved a surface temperature of 63.9 °C under 1 kW·m^{-2} illumination, which is significantly higher than that of both planar rGO-WC and planar rGO (Supplementary Figure 11a and 11b). The elevated EI temperature significantly enhanced the evaporation rate, so the solar evaporator with grid-like rGO-WC EI reached an evaporation rate of 2.31 kg·m^{-2}·h^{-1} for 3.5 wt% NaCl, which is also higher than that of the solar evaporator with planar rGO-WC EI and planar rGO EI, showing excellent photothermal conversion ability (Supplementary Figure 11c and 11d).



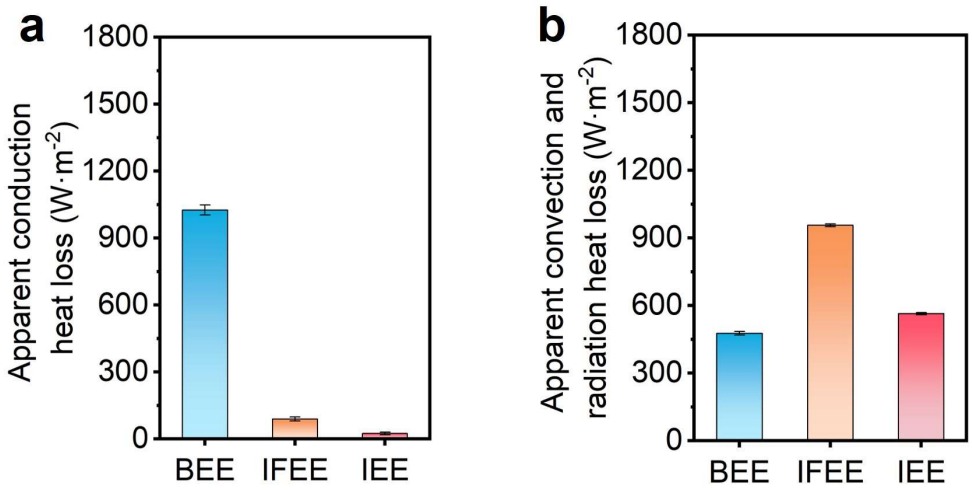
Supplementary Figure 12. Electrothermal performance of the IEE. (a) Evaporation rate and apparent energy efficiency of the IEE for 3.5 wt% NaCl under different input voltages. The data represent mean values ± SD (n = 3 independent experimental replicates). (b) Temperature changes in the IEE for 3.5 wt% NaCl under different input voltages. The data represent mean values ± SD (n = 3 independent experimental replicates). (c) Infrared thermal images of the IEE under different input voltages.



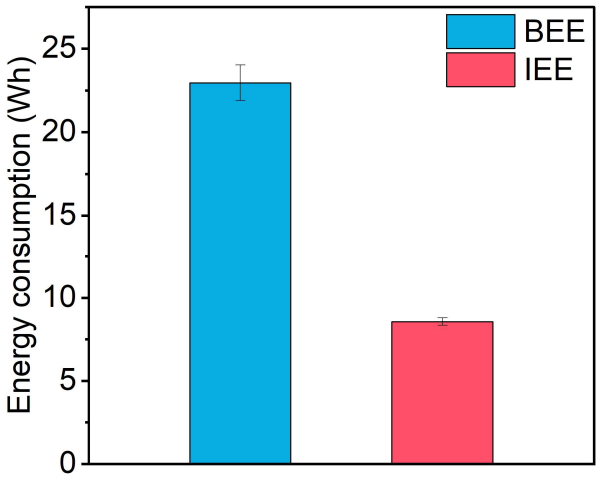
Supplementary Figure 13. Electrothermal performance of the electrothermal evaporator with the EL at the top or bottom. (a) Evaporation rate of the electrothermal evaporator with the EL at the top or bottom at 1.5 V. (b) Apparent energy efficiency and apparent heat loss of the electrothermal evaporator with the EL at the top or bottom after on the 10^{th} h at 1.5 V. The data represent mean values ± SD (n = 3 independent experimental replicates). (c) Schematic of the electrothermal evaporator with the EL at the top. (d) Cross-sectional infrared thermal image of the electrothermal evaporator with the EL at the top at 1.5 V. (e) Schematic of the electrothermal evaporator with the EL at the bottom. (f) Cross-sectional infrared thermal image of the electrothermal evaporator with the EL at the top at 1.5 V.



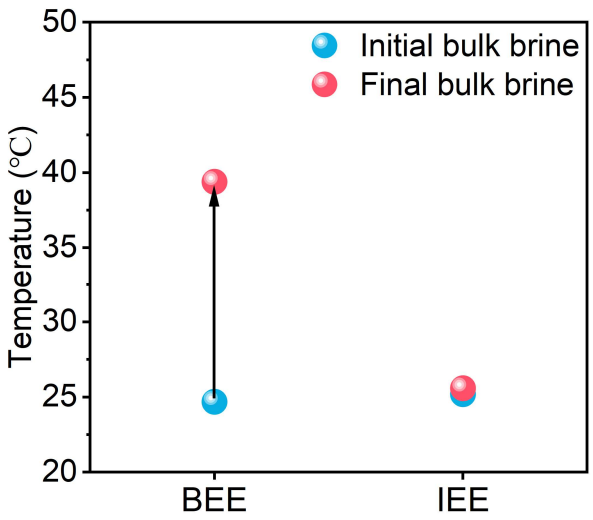
Supplementary Figure 14. Comparison of evaporation rate between IEE and traditional electrothermal evaporators at driving voltage.[23-31] The three differently sized asterisks denote the evaporation rates of the IEE at 0.5, 1, and 1.5 V, respectively.



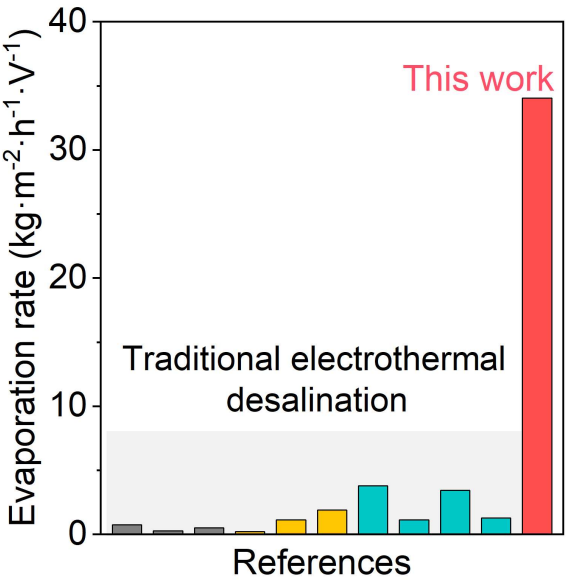
Supplementary Figure 15. Heat loss of BEE, IFEE, and IEE at 1.5 V. (a) Apparent conduction heat loss of BEE, IFEE, and IEE on the 10th h at 1.5 V. The data represent mean values ± SD (n = 3 independent experimental replicates). (b) Apparent convection and radiation heat loss of BEE, IFEE, and IEE on the 10th h at 1.5 V. The data represent mean values ± SD (n = 3 independent experimental replicates).



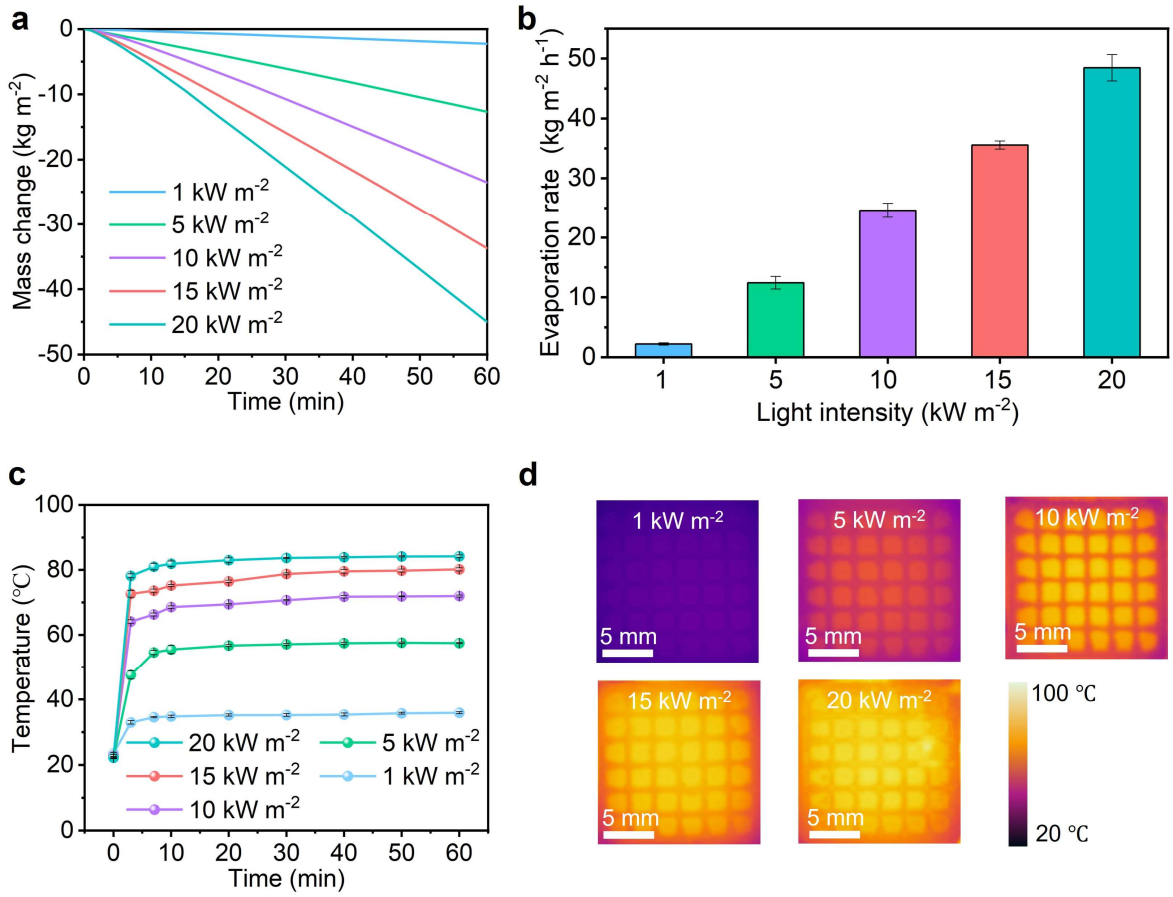
Supplementary Figure 16. Energy consumption of BEE and IEE at 1.5 V for evaporating 5 g of brine. The data represent mean values ± SD (n = 3 independent experimental replicates).



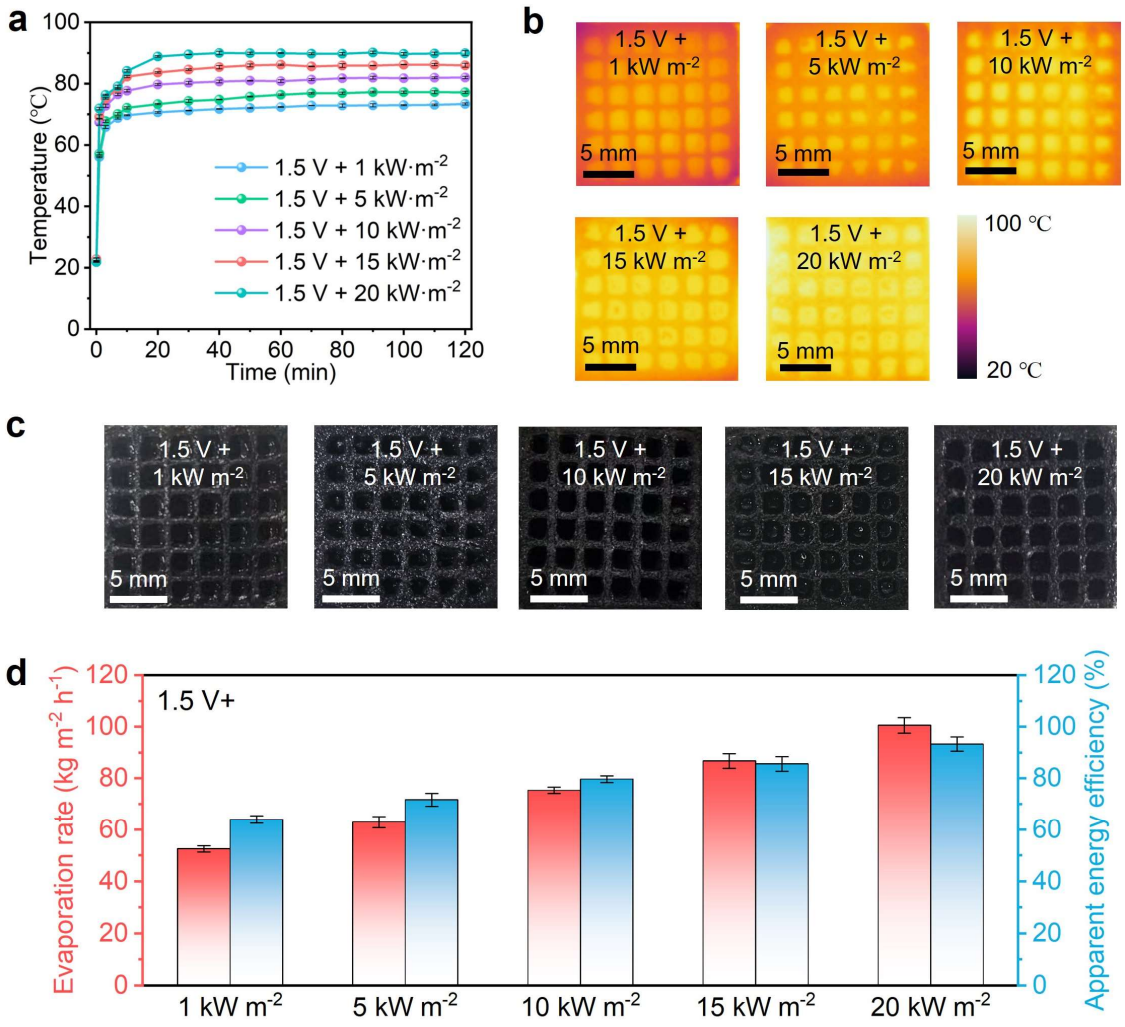
Supplementary Figure 17. Temperature changes of bulk brine in BEE and IEE.



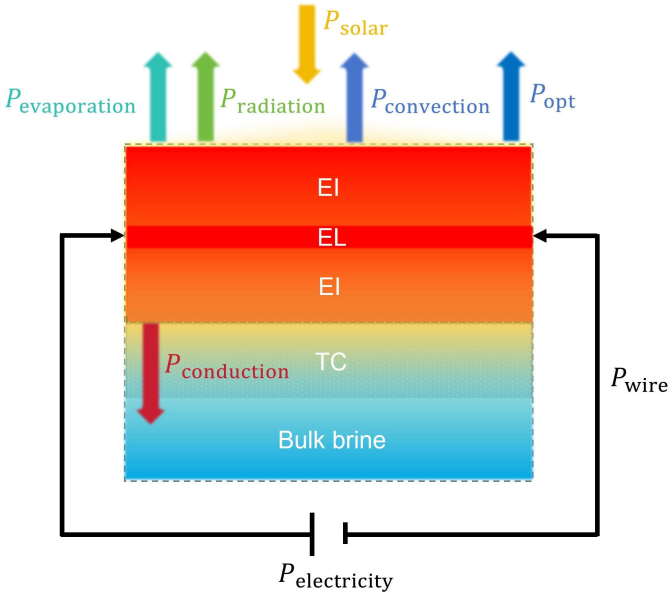
Supplementary Figure 18. Evaporation rate comparison between the IEE and previously reported electrothermal desalination technologies at unit voltage.[25,28,30-37]



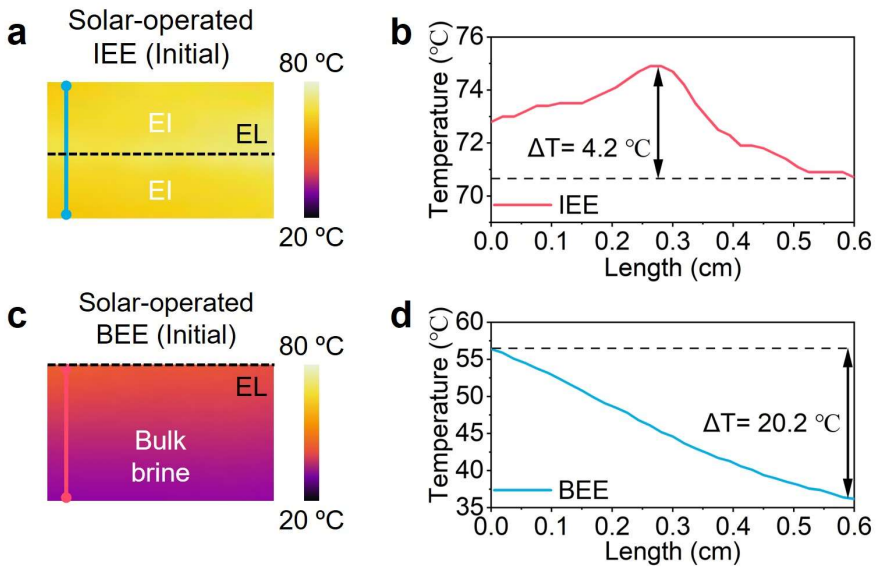
Supplementary Figure 19. Photothermal performance of the IEE under different light intensities. (a) Mass changes, (b) evaporation rates, (c) temperature changes, and of the IEE for 3.5 wt% NaCl under different light intensities. The data represent mean values ± SD (n = 3 independent experimental replicates). (d) Infrared thermal images of the IEE under different light intensities.



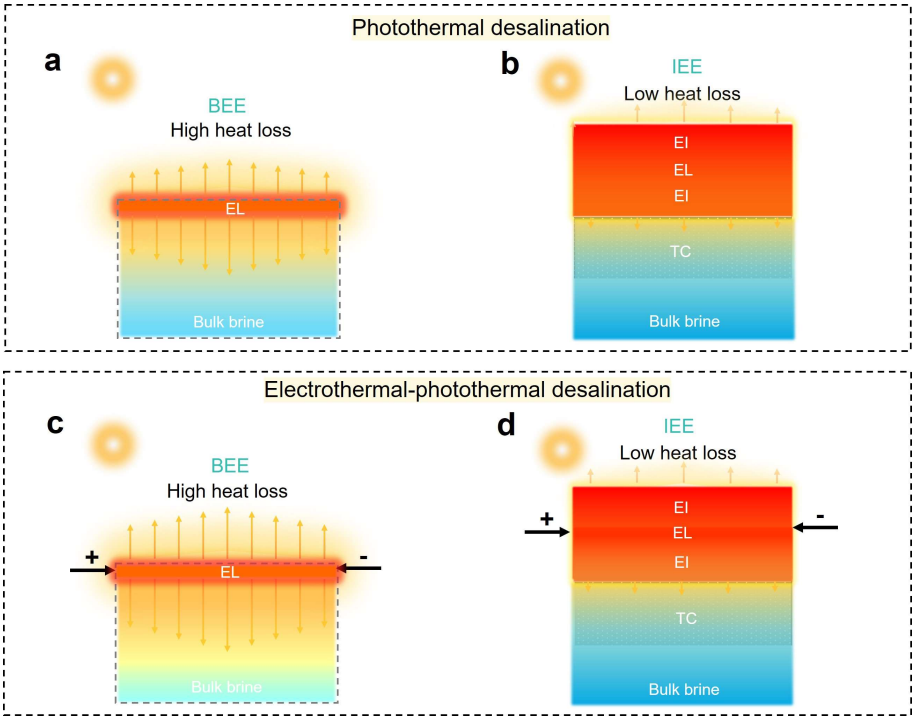
Supplementary Figure 20. Photothermal electrothermal coupling performance of the solar-operated IEE. (a) Temperature changes of the IEE for 3.5 wt% NaCl under different illumination and the voltage of 1.5 V. The data represent mean values ± SD (n = 3 independent experimental replicates). (b) Infrared images of the IEE at 60 min under different illumination and the voltage of 1.5 V. (c) Photographs of the EI in the IEE after the test. (d) Evaporation rates and apparent energy efficiency of the IEE for 3.5 wt% NaCl under different illumination and at the voltage of 1.5 V. The data represent mean values ± SD (n = 3 independent experimental replicates).



Supplementary Figure 21. Schematic of the heat transfer model for solar-operated IEE.

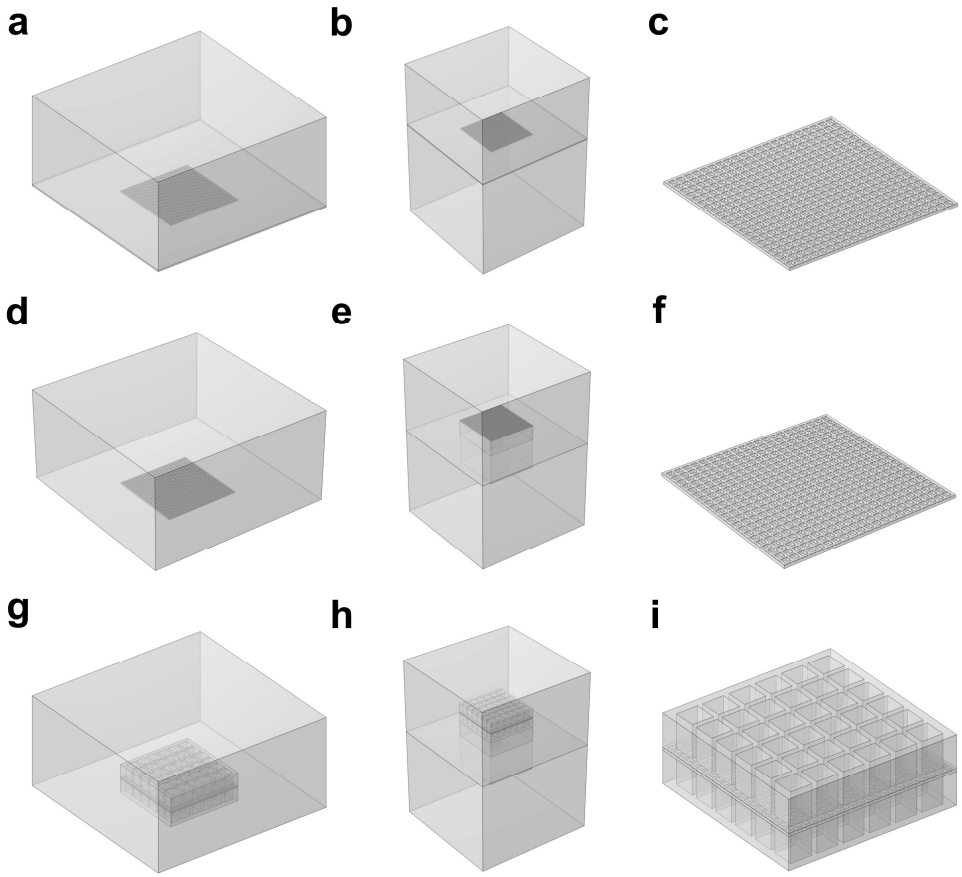


Supplementary Figure 22. Cross-sectional infrared thermal images and temperature distribution of the solar-operated IEE and BEE under 20 kW·m^{-2} illumination and at the voltage of 1.5 V. (a) Cross-sectional infrared thermal image of the solar-operated IEE at 1 min. (b) Cross-sectional temperature distribution of the solar-operated IEE at 1 min. (c) Cross-sectional infrared thermal image of the solar-operated BEE at 1 min. (d) Cross-sectional temperature distribution of the solar-operated BEE.

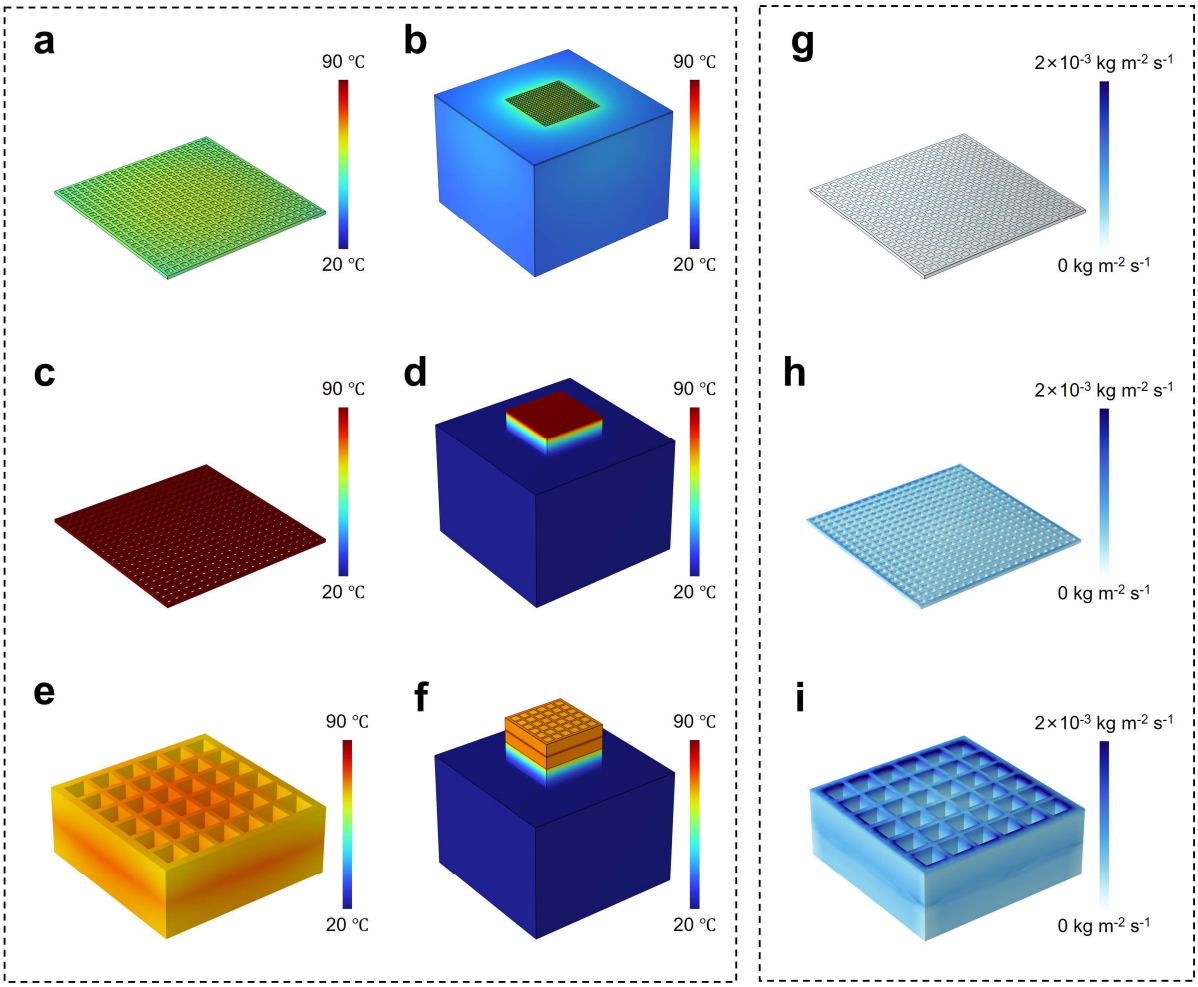


Supplementary Figure 23. Schematic of heat loss of BEE and IEE under electrothermal-photothermal conditions. Schematic of heat loss for photothermal desalination of (a) BEE and (b) IEE. Schematic of heat loss for electrothermal-photothermal desalination of (c) BEE and (d) IEE.

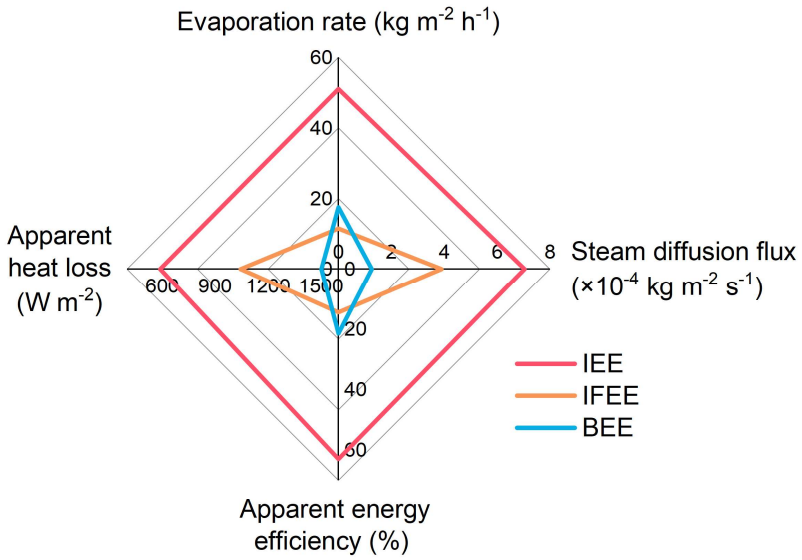
The solar-operated IEE exhibits excellent energy utilization efficiency for both electrical energy and solar energy simultaneously. Under purely photothermal conditions, solar-driven IEE with interface heating mode effectively reduces heat loss compared to the bulk photothermal evaporation of solar-driven BEE (Supplementary Figure 23a and Supplementary Figure 23b). Under coupled electrothermal-photothermal conditions, the above two energy utilization advantages are superimposed synergistically. The electrothermal layer and the evaporation interfaces work in tandem to convert both electrical energy and solar energy into evaporation energy with minimal heat loss (Supplementary Figure 23c and Supplementary Figure 23d). Therefore, the solar-operated IEE not only improves electrothermal evaporation performance but also provides a more efficient platform for solar energy utilization, leading to a more pronounced performance enhancement under solar irradiation.



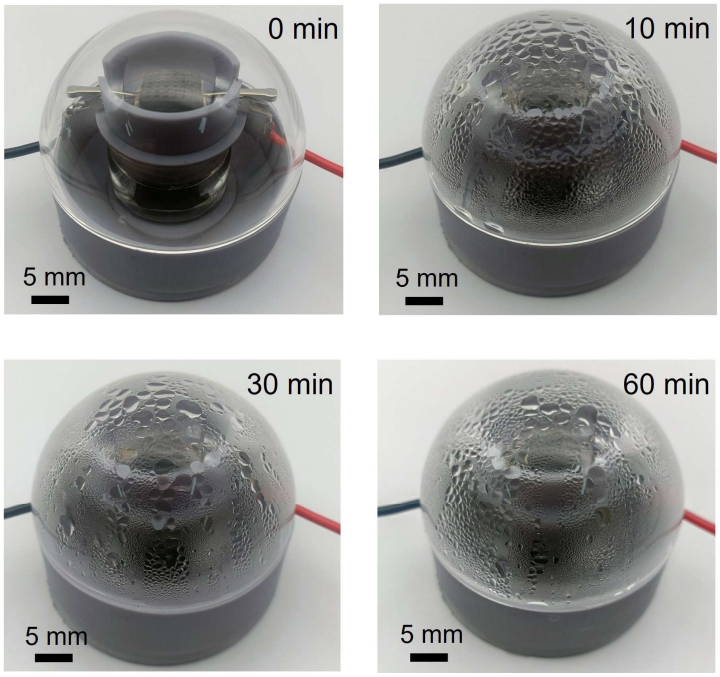
Supplementary Figure 24. Computation module of COMSOL simulations. (a) Model of the EL in BEE and environment as a whole. (b) Model of the BEE, bulk brine, and environment as a whole. (c) Model of the EL in BEE. (d) Model of the EL in IFEE and environment as a whole. (e) Model of the IFEE, bulk brine, and environment as a whole. (f) Model of the EL in IFEE. (g) Model of the EI in IEE and environment as a whole. (h) Model of the IEE, bulk brine, and environment as a whole. (i) Model of the EI in IEE.



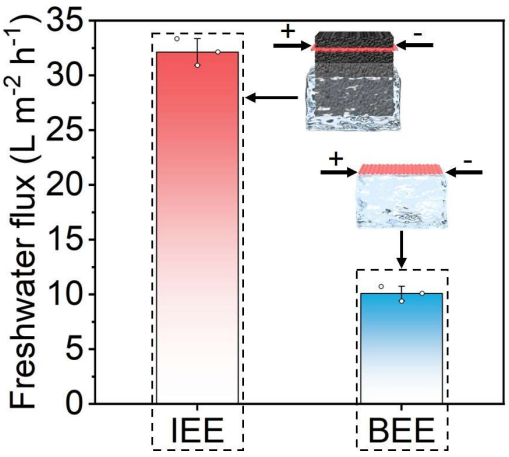
Supplementary Figure 25. COMSOL simulations of BEE, IFEE, and IEE. Theoretical simulation of BEE: (a) the temperature distribution for EL, (b) the temperature distribution for BEE, and (g) steam diffusion flux for the EL. Theoretical simulation of IFEE: (c) the temperature distribution for EL, (d) the temperature distribution for IFEE, and (h) steam diffusion flux for the EL. Theoretical simulation of IEE: (e) the temperature distribution for EI, (f) the temperature distribution for IEE, and (i) steam diffusion flux for the EI.



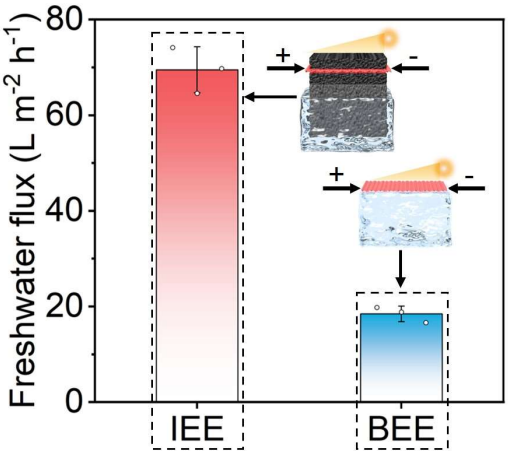
Supplementary Figure 26. Performance comparison of BEE, IFEE, and IEE in apparent energy efficiency, apparent heat loss, evaporation rate, and steam diffusion flux.



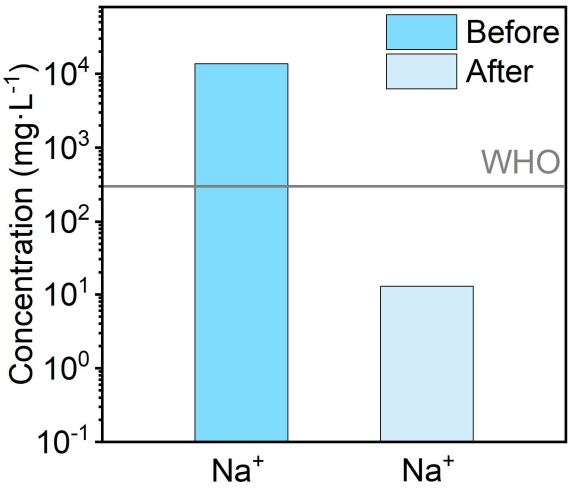
Supplementary Figure 27. Freshwater production phenomenon of the solar-operated IEE under 20 kW·m^{-2} illumination and at the voltage of 1.5 V.



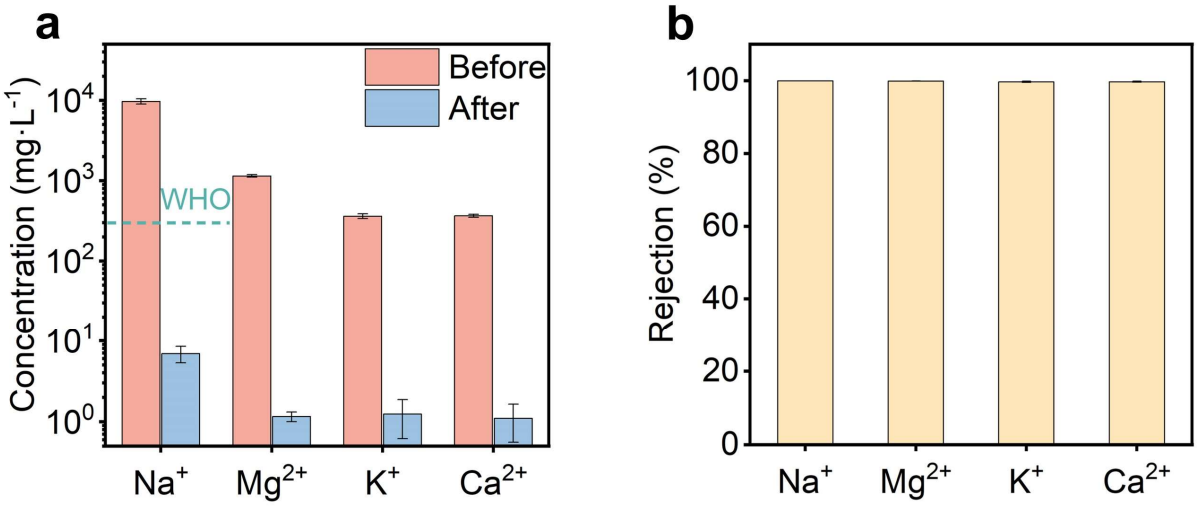
Supplementary Figure 28. Freshwater flux of IEE and BEE at 1.5 V. The data represent mean values ± SD (n = 3 independent experimental replicates).



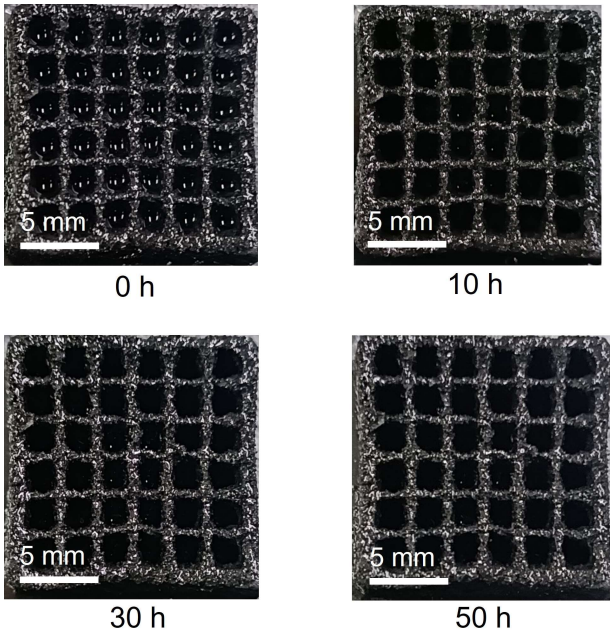
Supplementary Figure 29. Freshwater flux of the solar-operated IEE and solar-operated BEE. The data represent mean values ± SD (n = 3 independent experimental replicates).



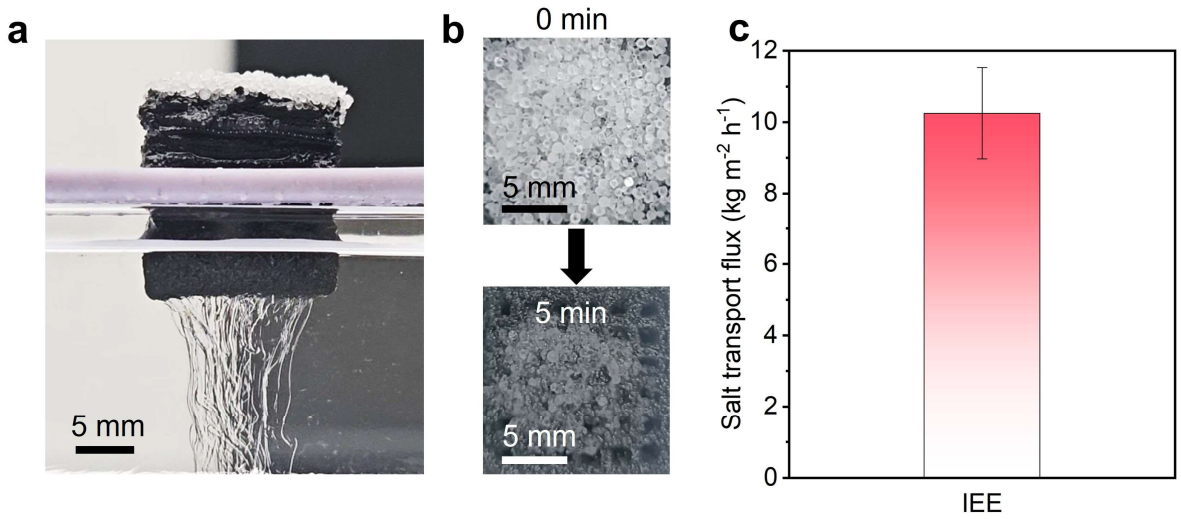
Supplementary Figure 30. Concentration changes in 3.5 wt% NaCl before and after solar desalination.



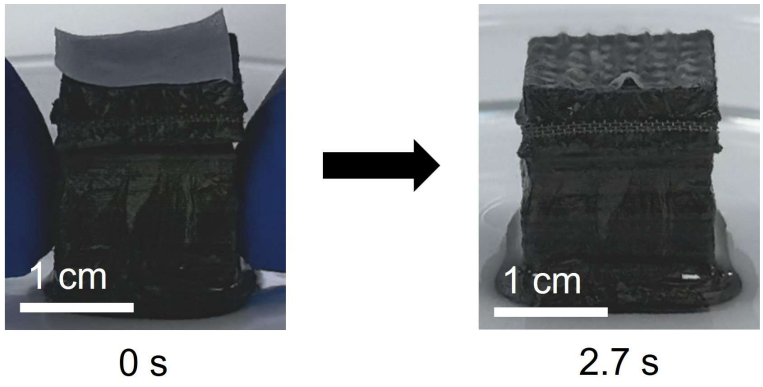
Supplementary Figure 31. Ion concentrations and rejection of IEE. (a) Ion concentrations of real Bohai seawater and freshwater collected by IEE. The data represent mean values ± SD (n = 3 independent experimental replicates). (b) Rejection of real Bohai seawater treated by IEE. The data represent mean values ± SD (n = 3 independent experimental replicates).



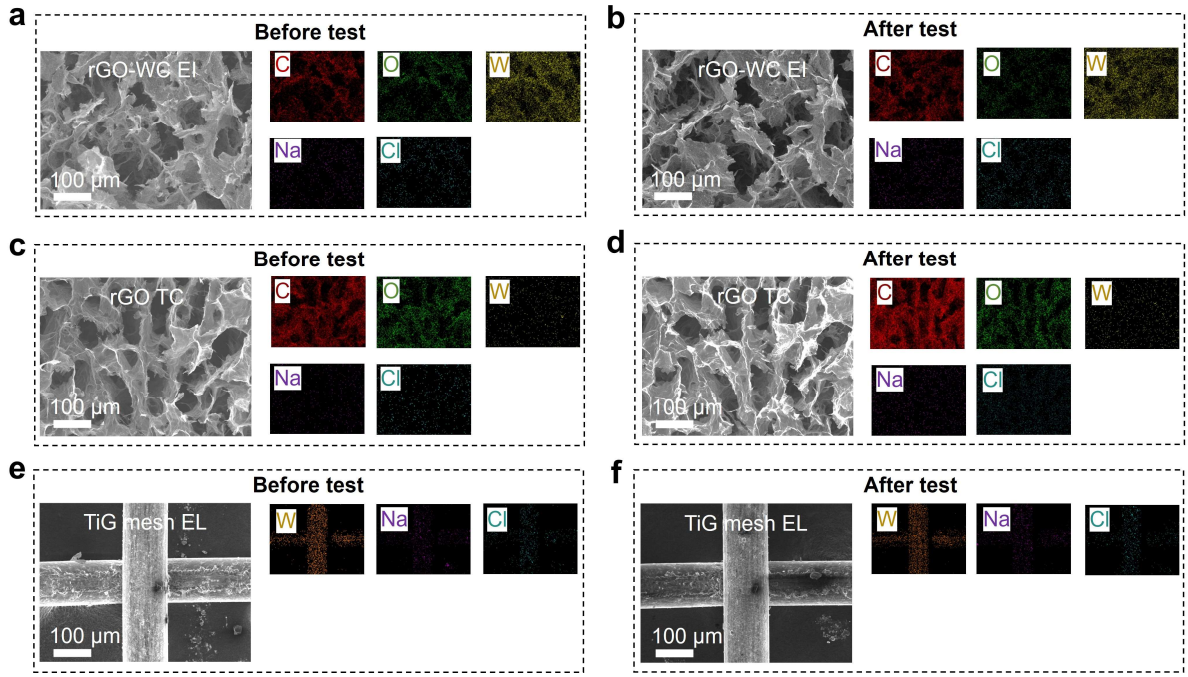
Supplementary Figure 32. Photographs of the solar-operated IEE during tests at different periods under 20 kW·m^{-2} illumination and at a voltage of 1.5 V.



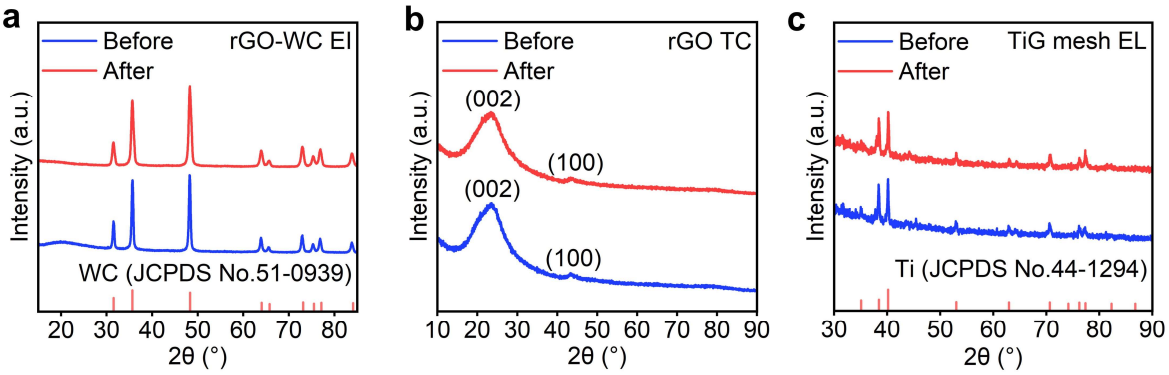
Supplementary Figure 33. Salt transport flux of the IEE. (a) Salt transport phenomenon of IEE. (b) Optical images of the IEE before and after salt transport flux measurement. (c) Salt transport flux of the IEE. The data represent mean values ± SD (n = 3 independent experimental replicates).



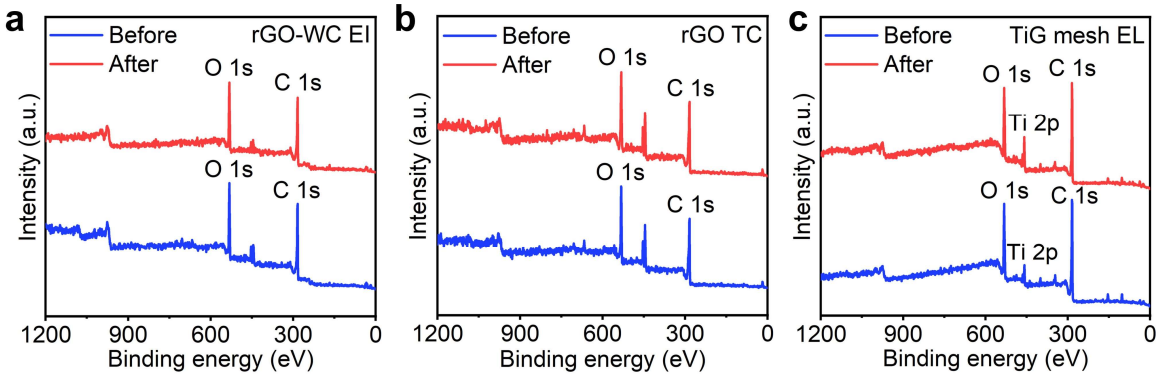
Supplementary Figure 34. Photographs of water transport for IEE.



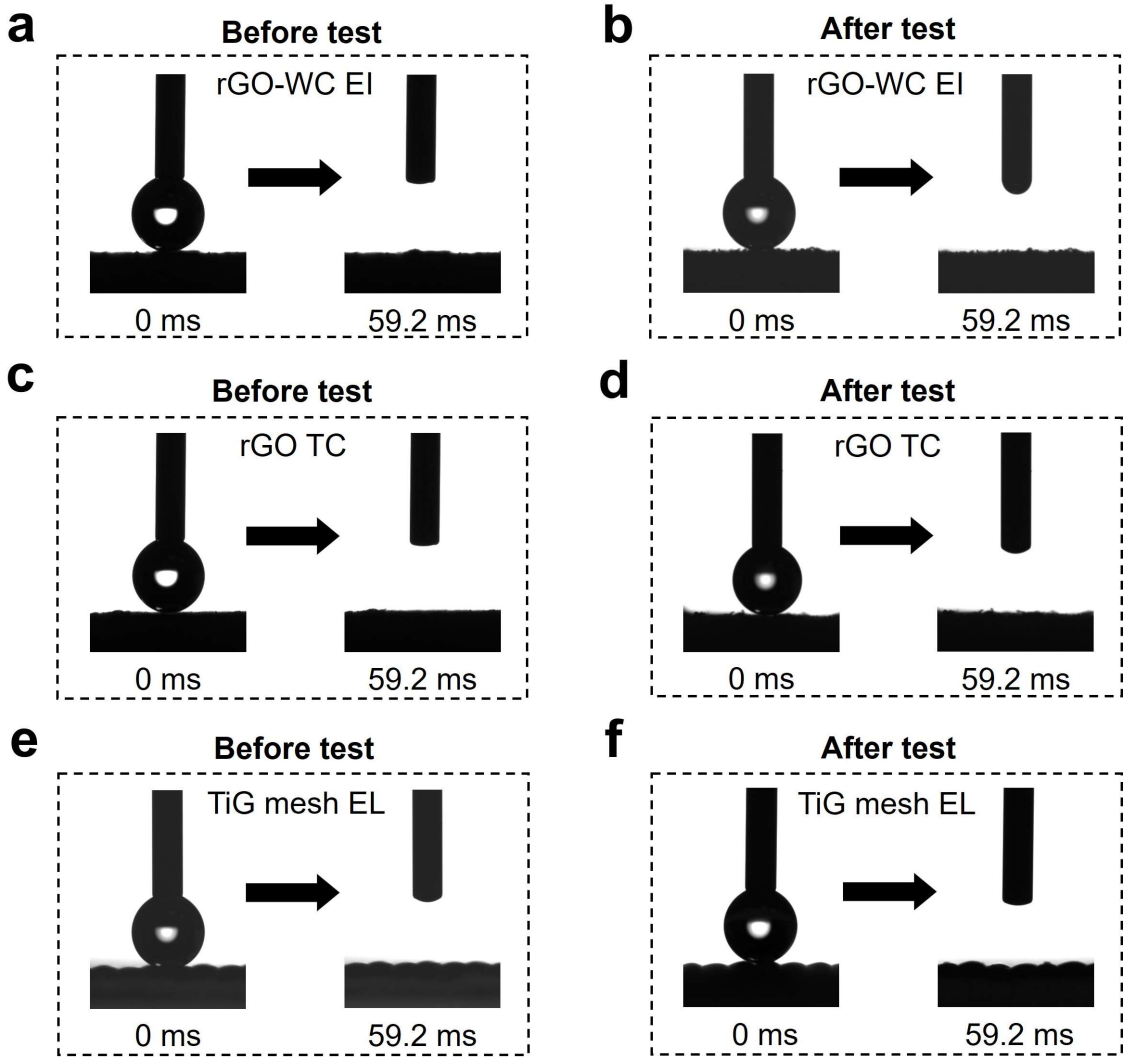
Supplementary Figure 35. SEM images and corresponding elemental mapping of rGO-WC EI of IEE (a) before and (b) after test. SEM images and corresponding elemental mapping of rGO TC of IEE (c) before and (d) after test. SEM images and corresponding elemental mapping of TiG mesh EL of IEE (e) before and (f) after test.



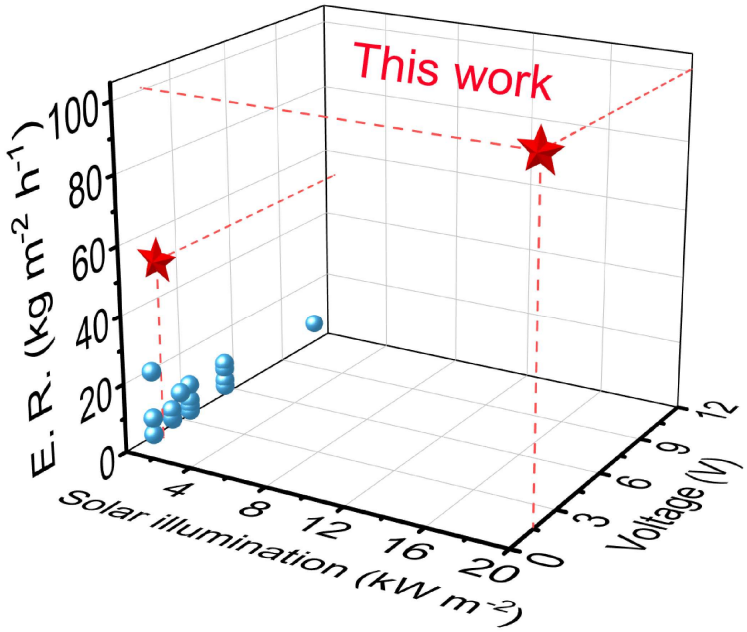
Supplementary Figure 36. (a) XRD patterns of rGO-WC EI of IEE before and after test. (b) XRD patterns of rGO TC of IEE before and after test. (c) XRD patterns of TiG mesh electrothermal layer of IEE before and after test.



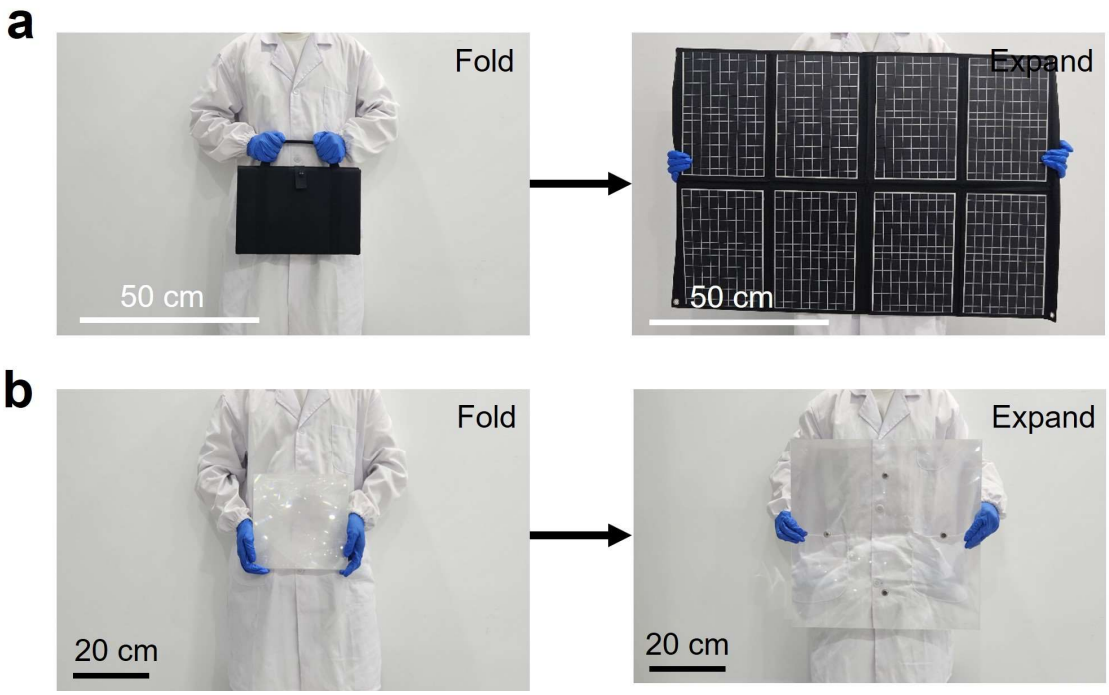
Supplementary Figure 37. (a) XPS spectra of rGO-WC EI of IEE before and after test. (b) XPS spectra of rGO TC of IEE before and after test. (c) XPS spectra of TiG mesh EL of IEE before and after test.



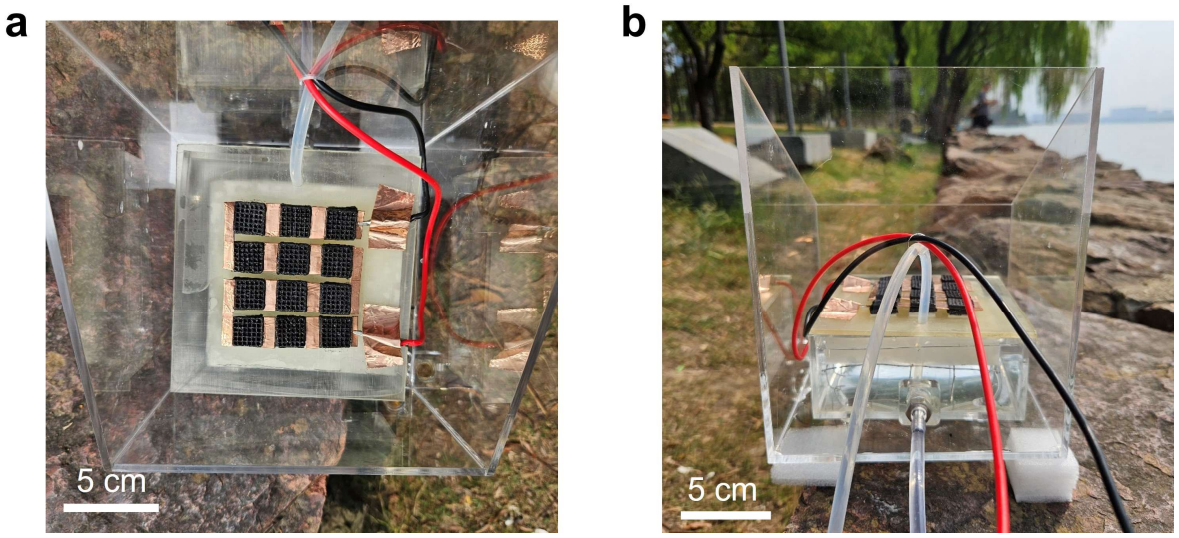
Supplementary Figure 38. (a) Water contact angle of rGO-WC EI of IEE before and after test. (b) Water contact angle of rGO TC of IEE before and after test. (c) Water contact angle of TiG mesh EL of IEE before and after test.



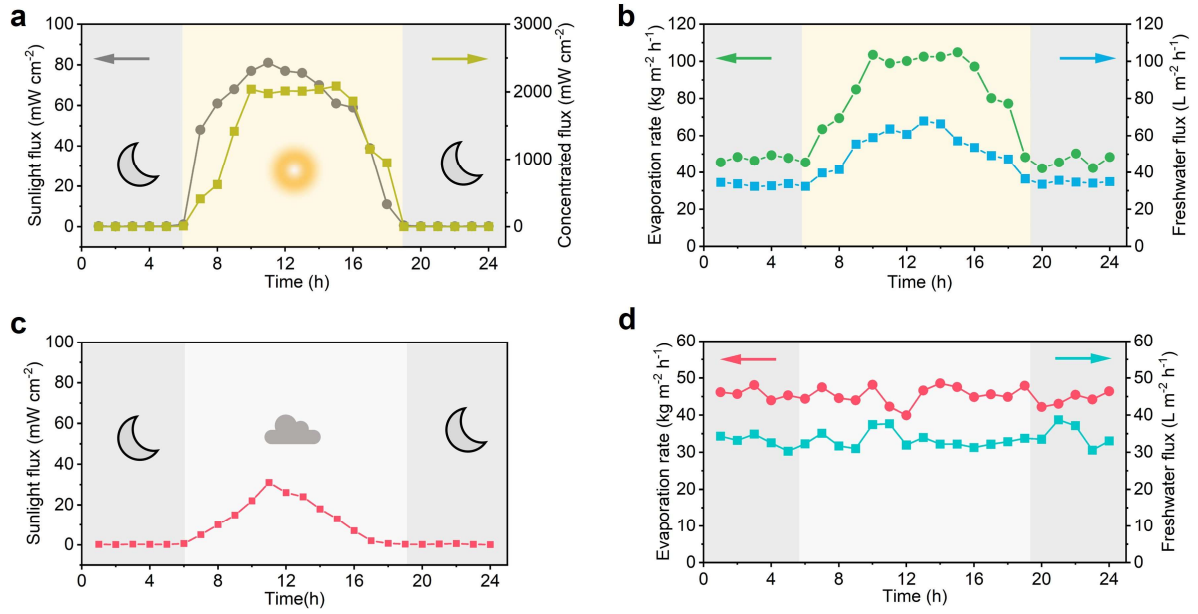
Supplementary Figure 39. Comparison of photothermal-electrothermal coupled evaporation rate between the solar-operated IEE (1.5 V with 1 kW·m^{-2} and 20 kW·m^{-2}) and other reported evaporators (details in Supplementary Table 5).[2,25,27-31,36-43]



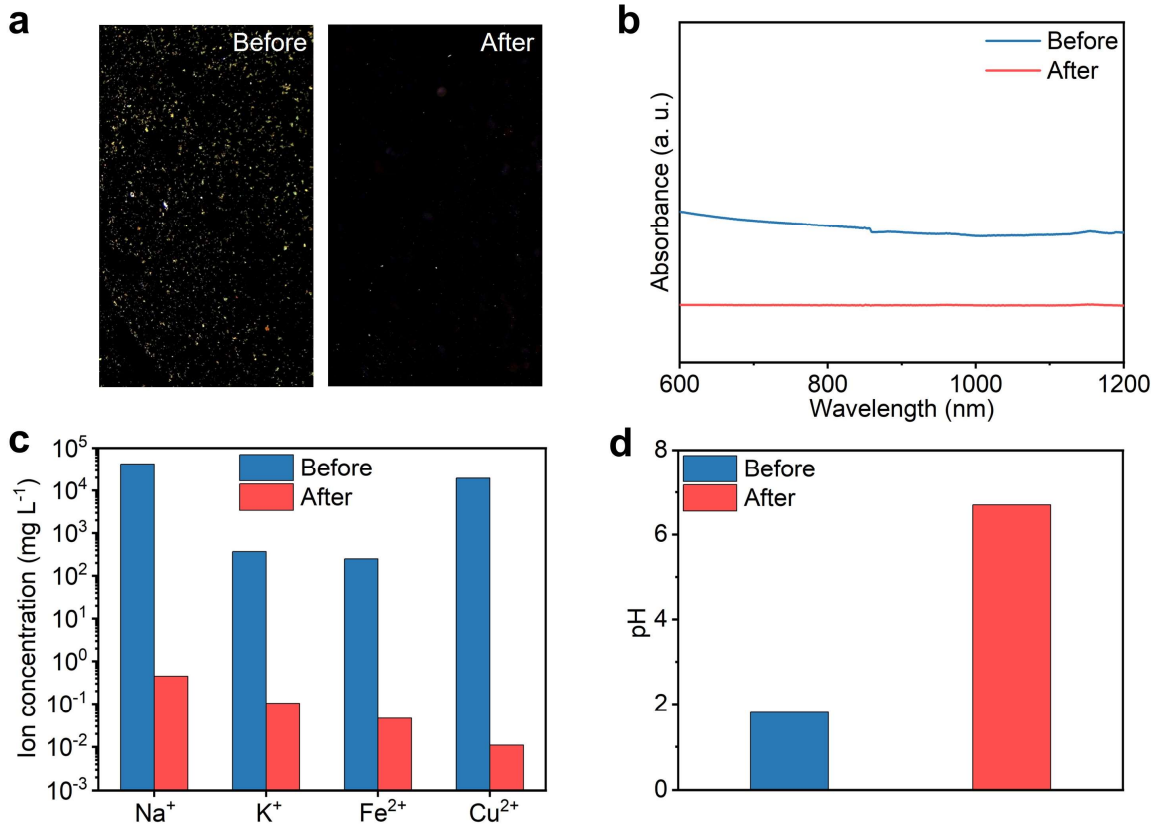
Supplementary Figure 40. Photographs of foldable solar cell and Fresnel lens. (a) Photograph of the folded and expanded solar cell. (b) Photograph of the folded and expanded Fresnel lens.



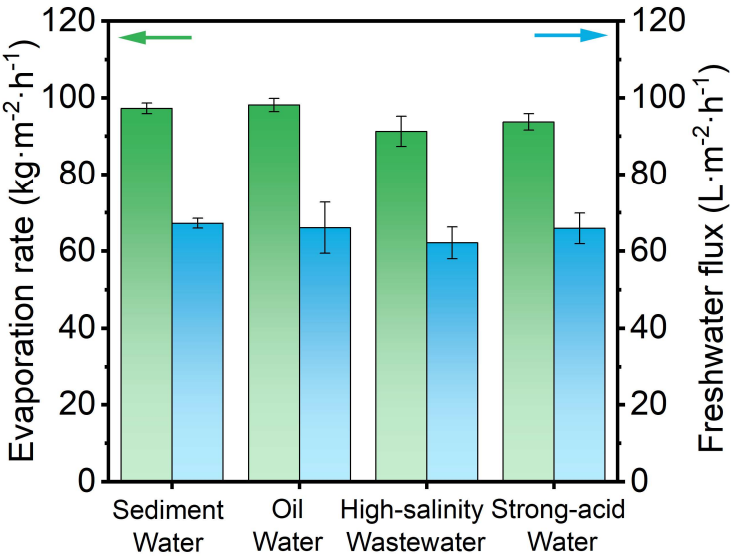
Supplementary Figure 41. Outdoor freshwater production and sample integration. (a) Photograph of the IEE integration. (b) Photograph of freshwater production device.



Supplementary Figure 42. All-day outdoor experiment. (a) The sunlight flux and the concentrated flux in Suzhou on February 18, 2025. (b) Evaporation rate and freshwater flux of the IEE for 3.5 wt% NaCl during the outdoor experiment in Suzhou on February 18, 2025. (c) Sunlight flux in Suzhou on January 23, 2025. (d) Evaporation rate and freshwater flux of the IEE for 3.5 wt% NaCl during the outdoor experiment in Suzhou on January 23, 2025.



Supplementary Figure 43. Characterization of various water sources before and after desalination. (a) Microscopic images of the sediment water before and after desalination. (b) Absorbance changes of the oil water before and after desalination. (c) Ion concentration changes of the high-salinity wastewater before and after desalination. (d) pH changes of the strong acid water before and after desalination.



Supplementary Figure 44. Evaporation rate and freshwater flux of the solar-operated IEE for sediment water, oil water, high-salinity wastewater, and strong-acid water under 20 kW·m^{-2} illumination and at the voltage of 1.5 V. The data represent mean values ± SD (n = 3 independent experimental replicates). The test results showed the evaporation rates of solar-operated IEE for sediment water, oily water, high-salinity wastewater, and strong-acid water treated were as high as 97.26, 98.12, 91.23, and 93.73 kg·m^{-2}·h^{-1} under 20 kW·m^{-2} illumination and at the voltage of 1.5 V, and the corresponding freshwater flux was as high as 67.22, 66.05, 62.14, and 65.89 L·m^{-2}·h^{-1}, showing excellent rapid freshwater production of multi-scenario water sources.

Supplementary Tables

Supplementary Table 1. Freshwater flux and apparent energy efficiency comparison of the IEE versus other reported electrothermal and photothermal desalination technologies.

Number	Type of desalination	Freshwater flux ($L \cdot m^{-2} \cdot h^{-1}$)	Apparent energy efficiency (%)	References
1	Electrothermal	6.78 (average)	39.33 (average)	2017 Nat. Nanotechnol.[44]
2		18.67 (average)	5.36 (average)	2018 Water Res.[45]
3		17.07 (average)	43.32 (average)	2020 Nat. Nanotechnol.[46]
4		4.18 (3 V)	22.47 (average)	2024 Adv. Sci.[2]
5	Photothermal	2.22	95.92	2023 Nature[10]
6		0.94 ± 0.12	59.8	2023 Nat. Water[47]
7		0.6	64.8	2025 Nat. Sustain.[48]
8		2.266	95.2	2025 Sci. Adv.[49]
9	**Photothermal-operated electrothermal**	**69.46**	**93.31**	**This work**

Supplementary Table 2. Comparison of evaporation rate between IEE and traditional electrothermal evaporator under different voltages.

Number	Voltage (V)	Evaporation rate ($kg \cdot m^{-2} \cdot h^{-1}$)	References
1	3	7.9	2025 Adv. Funct. Mater.[23]
2	3	4.50	2020 J. Mater. Chem. A[24]
3	2	2.26	2024 Chem. Eng. J.[25]
4	3	6.86	2022 J. Mater. Chem. A[26]
5	1	2.61	2022 Sci. China Mater.[27]
6	5	6.37	2026 ACS Nano[28]
7	10	5.00	2022 ACS Appl. Nano Mater.[30]
8	3	10.88	2024 Desalination[29]
9	5	0.99	2023 J. Mater. Chem. A[31]
10	**0.5**	**2.94**	
11	**1**	**15.94**	**This work**
12	**1.5**	**51.04**	

Supplementary Table 3. Evaporation rate comparison between the IEE and previously reported electrothermal desalination technologies at unit voltage.

Number	Materials	Evaporation rate ($kg \cdot m^{-2} \cdot h^{-1} \cdot V^{-1}$)	References
1	Carbon fiber/tencel composite braided yarn	0.76	2022 ACS Appl. Mater. Interfaces[32]
2	MGM@PVDF	0.28	2022 Chem. Eng. J.[33]
3	Laser-induced graphene	0.50	2022 ACS Appl. Nano Mater.[30]
4	ANF/CNT/PPy	0.20	2023 J. Mater. Chem. A[31]
5	Zeolite-chitosan-TiO_2@PPy aerogel	1.14	2023 Chem. Eng. J.[34]
6	Wood-derived all-carbon conductive foam	1.90	2023 Mater. Today Nano[36]
7	CNTs/PAAm hydrogel	3.79	2024 Nano Energy[37]
8	Cotton cloth/PPy/heating wires/acrylamide hydrogel	1.13	2024 Chem. Eng. J.[25]
9	Cu/CuO-PPy	3.42	2024 J. Mater. Chem. A[35]
10	PVA/MS/BG/ Fe-Cr-Al alloy wires	1.27	2026 ACS Nano[28]
11	**rGO-WC/TiG mesh/rGO**	**34.03**	**This work**

Supplementary Table 4. ICP data of ion concentration of real Bohai seawater and collected freshwater.

Water source	Concentration of Na^+ (mg L^{-1})	Concentration of Mg^{2+} (mg L^{-1})	Concentration of K^+ (mg L^{-1})	Concentration of Ca^{2+} (mg L^{-1})
Bohai seawater	9701.38	1144.70	361.95	365.97
Collected Freshwater	6.90	1.16	1.24	1.10

Supplementary Table 5. Comparison of photothermal-electrothermal coupled evaporation rate between IEE and other reported evaporators.

Number	Voltage (V)	Solar illumination ($kW \cdot m^{-2}$)	Evaporation rate ($kg \cdot m^{-2} \cdot h^{-1}$)	References
1	5	1	6.53	2021 Nano Energy [38]
2	1	1	2.61	2022 Sci. China Mater.[27]
3	2.5	0.5	1.62	2022 Mater. Horiz.[39]
4	2	1	6.73	2023 Mater. Today Nano[36]
5	10	1.5	10.25	2022 Solar RRL[50]
6	5	1	11.70	2023 Chem. Eng. J.[34]
7	3	1	3.40	2024 Chem. Eng. J.[40]
8	5	1	10.05	2026 ACS Nano[28]
9	3	1	4.89	2024 Adv. Sci.[2]
10	1	1	7.43	2024 Nano Energy[37]
11	2.5	1	10.37	2024 Appl. Surf. Sci.[41]
12	3	1	11.20	2024 Desalination[29]
13	1	1	21.30 ± 3.60	2024 Desalination[42]
14	5	1	4.71	2023 J. Mater. Chem. A[31]
15	2	1	4.58	2024 Chem. Eng. J.[25]
16	3	1	6.60	2024 Nano Lett.[43]
17	**1.5**	**1**	**52.58**	**This work**
18	**1.5**	**20**	**100.66**	

Supplementary Table 6. Natural and concentrated light intensities change with time in Suzhou on August 19, 2025.

Time	Natural light intensity ($kW \cdot m^{-2}$)	Concentrated light intensity by lens ($kW \cdot m^{-2}$)
9:00	0.87	20.45
10:00	1.00	20.75
11:00	1.04	21.14
12:00	1.07	21.67
13:00	1.02	21.50
14:00	0.96	20.80
15:00	0.89	20.62
16:00	0.82	20.35

Supplementary Table 7. Comparison of freshwater flux with other reported water treatment technologies.

Number	Type	Material or design	Treated solution	Concentration of NaCl (wt%)	Freshwater flux ($L \cdot m^{-2} \cdot h^{-1}$)	References
1	Reverse osmosis	TFC-HC6	35,000 ppm NaCl	3.5	75	2020, Nat. Nanotechnol.[51]
2	Reverse osmosis	TA-RO	2000 ppm NaCl	0.2	31.65 ± 0.21	2025, Nat. Water[52]
3	Reverse osmosis	M-CDs-0.1	3000 ppm NaCl	0.3	18.32	2026, Nat. Commun.[53]
4	Membrane distillation	Wood	1 $g \cdot L^{-1}$ NaCl	0.1	20.8 ± 0.8	2019, Sci. Adv.[54]
5	Membrane distillation	NF-PES-8	35 $g \cdot L^{-1}$ NaCl	3.5	24.8	2023, Nat. Commun.[55]
6	Membrane distillation	PTFE NFMs	3.5 wt% NaCl	3.5	52.1	2024, Water. Res.[56]
7	**Solar-operated IEE**	**rGO-WC/Ti mesh/rGO**	**3.5 wt% NaCl**	**3.5**	**69.46 (laboratory) 66.72 (outdoors)**	**This work**

Supplementary references

1 Ghasemi, H. et al. Solar steam generation by heat localization. *Nat. Commun.* **5**, 4449 (2014).

2 Xu, D. et al. Photo-electro-thermal textiles for scalable, high-performance, and salt-resistant solar-driven desalination. *Adv. Sci.* **11**, 2400623 (2024).

3 Wang, M. et al. Alternative photothermal/electrothermal hierarchical membrane for hypersaline water treatment. *SusMat* **2**, 679-688 (2022).

4 Xu, J. et al. Charge-transfer cocrystal via a persistent radical cation acceptor for efficient solar-thermal conversion. *Angew. Chem. Int. Ed.* **61**, e202202571 (2022).

5 Liu, J. et al. Donor-acceptor molecule based high-performance photothermal organic material for efficient water purification and electricity generation. *Angew. Chem. Int. Ed.* **61**, e202117087 (2022).

6 Cheng, P. et al. Synergizing plasmonic local heating and 3D nanostructures to boost the solar-to-vapor efficiency beyond 100%. *Adv. Mater.* **37**, 2415655 (2025).

7 Li, Y. et al. High-entropy-alloy-nanoparticles enabled wood evaporator for efficient photothermal conversion and sustainable solar desalination. *Adv. Energy Mater.* **12**, 2203057 (2022).

8 Zhao, G. et al. Engineering high-tortuosity 3D gradient structure and CFD-assisted multifield analysis for solar interfacial evaporation. *Small* **20**, 2305855 (2024).

9 Xu, K. et al. Teardrop-shaped 3D solar evaporator with multiscale biomimetic water-supply structures for highly efficient seawater desalination. *Adv. Funct. Mater.* **36**, e20574 (2026).

10 Yang, B. et al. Flatband λ-Ti_3O_5 towards extraordinary solar steam generation. *Nature* **622**, 499-506 (2023).

11 Zhang, H., Duan, Y., Elimelech, M. & Wang, Y. Scalable catalytic nanofiltration membranes for advanced water treatment. *Nat. Water* **3**, 1038-1047 (2025).

12 Zhang, S. et al. Solar-driven membrane separation for direct lithium extraction from artificial salt-lake brine. *Nat. Commun.* **15**, 238 (2024).

13 Yang, H. et al. Tailoring the salt transport flux of solar evaporators for a highly effective

salt-resistant desalination with high productivity. *ACS Nano* **16**, 2511-2520 (2022).

14 Yang, H. et al. High freshwater flux solar desalination via a 3D plasmonic evaporator with an efficient heat-mass evaporation interface. *Adv. Mater.* **35**, 2304699 (2023).

15 Xu, Y. et al. All-in-one polymer sponge composite 3D evaporators for simultaneous high-flux solar-thermal desalination and electricity generation. *Nano Energy* **93**, 106882 (2022).

16 Xu, W. et al. Efficient water transport and solar steam generation via radially, hierarchically structured aerogels. *ACS Nano* **13**, 7930-7938 (2019).

17 Zou, H. et al. Harnessing multiple Donnan effects for simultaneous salt-resistant solar desalination and dual-mode power generation. *Adv. Mater.* **38**, e73163 (2026).

18 Cao, Y. et al. Spatially regulated water-heat transport by fluidic diode membrane for efficient solar-powered desalination and electricity generation. *Nat. Commun.* **16**, 5050 (2025).

19 Xu, J. et al. All-in-one hybrid atmospheric water harvesting for all-day water production by natural sunlight and radiative cooling. *Energy Environ. Sci.* **17**, 4988-5001 (2024).

20 Guo, Y. et al. Latent heat-assisted cooling for high-efficiency solar-driven freshwater production. *Nat. Commun.* **16**, 11709 (2025).

21 Liu, C. et al. Ultralow-density rigid network hydrogels enable ultrafast and stable solar water desalination. *Nat. Commun.* **17**, 5822 (2026).

22 Sun, L. et al. A robust solar evaporator with hierarchical architecture for ultrahigh efficiency and large-scale zero-liquid-discharge desalination. *Adv. Sci.* **13**, e17735 (2026).

23 Li, X. et al. Biomimetic design of photothermal/electrothermal fabric composed of carbon-core/nanorod-array-shell fibers for efficient all-weather seawater evaporation. *Adv. Funct. Mater.* **35**, 2423472 (2025).

24 Guo, Y., Sui, Y., Zhang, J., Cai, Z. & Xu, B. An all-day solar-driven vapor generator via photothermal and Joule-heating effects. *J. Mater. Chem. A* **8**, 25178-25186 (2020).

25 Fang, H. et al. Electrothermal-assisted all-weather solar steam generator based on hydrogel implantation strategy. *Chem. Eng. J.* **494**, 153110 (2024).

26 Liu, F. et al. Electrically powered artificial black body for low-voltage high-speed

interfacial evaporation. *J. Mater. Chem. A* **10**, 22992-23000 (2022).

27 Sun, S. et al. Fabric-based all-weather-available photo-electro-thermal steam generator with high evaporation rate and salt resistance. *Sci. China Mater.* **65**, 2479-2490 (2022).

28 Wang, M. et al. Energy-harvesting evaporator mimics photosynthesis-respiration cycle and enables all-day seawater desalination. *ACS Nano* **20**, 7249-7259 (2026).

29 Pandit, T. P., Wilson, H. M. & Lee, S. J. Joule-heating assisted heliotropic solar steam generator for all-day, all-weather solar desalination. *Desalination* **573**, 117185 (2024).

30 Barbhuiya, N. H., Misra, U. & Singh, S. P. Stacked laser-induced graphene Joule heaters for desalination and water recycling. *ACS Appl. Nano Mater.* **5**, 10991-11002 (2022).

31 Wang, M. et al. Aramid-based aerogels for driving water evaporation through both photo-thermal and electro-thermal effects. *J. Mater. Chem. A* **11**, 7711-7723 (2023).

32 Xu, D. et al. Composite braided fabric coupled with photothermal and electrothermal processes for stable and continuous all-day desalination. *ACS Appl. Mater. Interfaces* **14**, 52087-52095 (2022).

33 Zhang, J. et al. Monolithic all-weather solar-thermal interfacial membrane evaporator. *Chem. Eng. J.* **450**, 137893 (2022).

34 Zhao, S., Zhang, X., Wei, G. & Su, Z. All-weather photothermal-electrothermal integrated system for efficient solar steam generation. *Chem. Eng. J.* **458**, 141520 (2023).

35 Chen, M. et al. 3D bridge-arch-structured dual-side evaporator for practical, all-weather water harvesting and desalination. *J. Mater. Chem. A* **12**, 9574-9583 (2024).

36 Wang, F. et al. Natural wood-derived all-carbon-conductive foam for sustainable all-weather monolithic photo-electrothermal interfacial water evaporation. *Mater. Today Nano* **23**, 100352 (2023).

37 Qiu, J. et al. A solar-electric dual-driven microporous hydrogel evaporator for all-weather highly efficient water purification. *Nano Energy* **130**, 110057 (2024).

38 Li, L. & Zhang, J. Highly salt-resistant and all-weather solar-driven interfacial evaporators with photothermal and electrothermal effects based on Janus graphene@silicone sponges. *Nano Energy* **81**, 105682 (2021).

39 Zhao, X. et al. All-weather-available, continuous steam generation based on the

synergistic photo-thermal and electro-thermal conversion by MXene-based aerogels. *Mater. Horiz.* **7**, 855-865 (2020).

40 Ge, C. et al. Film-twist-yarn evaporator with durable salt resistance for efficient photo-electro-thermal desalination. *Chem. Eng. J.* **486**, 150303 (2024).

41 Pu, G. et al. Enhanced interfacial evaporation of CF@NC fabric via coupled photo-thermal and Joule-heating effect. *Appl. Surf. Sci.* **661**, 160097 (2024).

42 Patra, A. S., Lim, H. W., Arunkumar, T. & Lee, S. J. A robust photoelectrothermal evaporator with hierarchical $NiCo_2S_4$ nanowires grown on nickel foam for a high rate of clean water production. *Desalination* **592**, 118074 (2024).

43 Yan, J. et al. In situ MXene anchored structure for highly durable solar steam generation. *Nano Lett.* **24**, 3515-3524 (2024).

44 Dudchenko, A. V., Chen, C., Cardenas, A., Rolf, J. & Jassby, D. Frequency-dependent stability of CNT Joule heaters in ionizable media and desalination processes. *Nat. Nanotechnol.* **12**, 557-563 (2017).

45 Qin, W. et al. Comparison of colloidal silica involved fouling behavior in three membrane distillation configurations using PTFE membrane. *Water Res.* **130**, 343-352 (2018).

46 Zuo, K. et al. Multifunctional nanocoated membranes for high-rate electrothermal desalination of hypersaline waters. *Nat. Nanotechnol.* **15**, 1025-1032 (2020).

47 Pornrungroj, C. et al. Hybrid photothermal-photocatalyst sheets for solar-driven overall water splitting coupled to water purification. *Nat. Water* **1**, 952-960 (2023).

48 Chen, Y. et al. Large-scale implementation of solar interfacial desalination. *Nat. Sustain.* **8**, 162-169 (2025).

49 Liu, Y. et al. Strong interaction between plasmon and topological surface state in $Bi_2Se_3/Cu_{2-x}S$ nanowires for solar-driven photothermal applications. *Sci. Adv.* **11**, eadt2884 (2025).

50 Su, J., Chang, Q., Xue, C., Yang, J. & Hu, S. Sponge-supported reduced graphene oxides enable synergetic photothermal and electrothermal conversion for water purification coupling hydrogen peroxide production. *Solar RRL* **6**, 2200767 (2022).

51 Di Vincenzo, M. et al. Biomimetic artificial water channel membranes for enhanced

desalination. *Nat. Nanotechnol.* **16**, 190-196 (2021).

52 Liu, Y. et al. Sustainable polyester thin films for membrane desalination developed through interfacial catalytic polymerization. *Nat. Water* **3**, 430-438 (2025).

53 Shao, X. et al. Overcoming the trade-off in reverse osmosis membranes through homologous matching. *Nat. Commun.* **17**, 2308 (2026).

54 Hou, D. et al. Hydrophobic nanostructured wood membrane for thermally efficient distillation. *Sci. Adv.* **5**, eaaw3203 (2019).

55 Hou, Y. et al. A super liquid-repellent hierarchical porous membrane for enhanced membrane distillation. *Nat. Commun.* **14**, 6886 (2023).

56 Liu, Y. et al. Crosslinking and fluorination reinforced PTFE nanofibrous membrane with excellent amphiphobic performance for low-scaling membrane distillations. *Water Res.* **256**, 121594 (2024).